AFRL-RI-RS-TR-2020-185

DEVELOPMENT OF A WIDE-BANDGAP PROGRAMMABLE NANOPHOTONIC PROCESSOR

MASSACHUSETTS INSTITUTE OF TECHNOLOGY

OCTOBER 2020

FINAL TECHNICAL REPORT

APPROVED FOR PUBLIC RELEASE; DISTRIBUTION UNLIMITED

STINFO COPY

AIR FORCE RESEARCH LABORATORY
INFORMATION DIRECTORATE

■ **AIR FORCE MATERIEL COMMAND** ■ **UNITED STATES AIR FORCE** ■ **ROME, NY 13441**

NOTICE AND SIGNATURE PAGE

Using Government drawings, specifications, or other data included in this document for any purpose other than Government procurement does not in any way obligate the U.S. Government. The fact that the Government formulated or supplied the drawings, specifications, or other data does not license the holder or any other person or corporation; or convey any rights or permission to manufacture, use, or sell any patented invention that may relate to them.

This report is the result of contracted fundamental research deemed exempt from public affairs security and policy review in accordance with SAF/AQR memorandum dated 10 Dec 08 and AFRL/CA policy clarification memorandum dated 16 Jan 09. This report is available to the general public, including foreign nations. Copies may be obtained from the Defense Technical Information Center (DTIC) (http://www.dtic.mil).

AFRL-RI-RS-TR-2020-185 HAS BEEN REVIEWED AND IS APPROVED FOR PUBLICATION IN ACCORDANCE WITH ASSIGNED DISTRIBUTION STATEMENT.

FOR THE CHIEF ENGINEER:

/ S /
KRISTI MEZZANO
Work Unit Manager

/ S /
GREGORY HADYNSKI
Assistant Technical Advisor
Computing & Communications Division
Information Directorate

This report is published in the interest of scientific and technical information exchange, and its publication does not constitute the Government's approval or disapproval of its ideas or findings.

REPORT DOCUMENTATION PAGE

Form Approved
OMB No. 0704-0188

1. REPORT DATE *(DD-MM-YYYY)*	2. REPORT TYPE	3. DATES COVERED *(From - To)*
OCTOBER 2020	FINAL TECHNICAL REPORT	MAR 2016 – MAR 2020

4. TITLE AND SUBTITLE

DEVELOPMENT OF A WIDE-BANDGAP PROGRAMMABLE NANOPHOTONIC PROCESSOR

5a. CONTRACT NUMBER
FA8750-16-2-0141

5b. GRANT NUMBER
N/A

5c. PROGRAM ELEMENT NUMBER
62788F

6. AUTHOR(S)

Dirk R. Englund

5d. PROJECT NUMBER
ARAP

5e. TASK NUMBER
UM

5f. WORK UNIT NUMBER
IT

7. PERFORMING ORGANIZATION NAME(S) AND ADDRESS(ES)
Massachusetts Institute of Technology
Research Laboratory of Electronics (RLE)
77 Massachusetts Avenue
Cambridge, MA 02139

8. PERFORMING ORGANIZATION REPORT NUMBER

9. SPONSORING/MONITORING AGENCY NAME(S) AND ADDRESS(ES)

Air Force Research Laboratory/RITQ
525 Brooks Road
Rome NY 13441-4505

10. SPONSOR/MONITOR'S ACRONYM(S)
AFRL/RI

11. SPONSOR/MONITOR'S REPORT NUMBER
AFRL-RI-RS-TR-2020-185

12. DISTRIBUTION AVAILABILITY STATEMENT
Approved for Public Release; Distribution Unlimited. This report is the result of contracted fundamental research deemed exempt from public affairs security and policy review in accordance with SAF/AQR memorandum dated 10 Dec 08 and AFRL/CA policy clarification memorandum dated 16 Jan 09.

13. SUPPLEMENTARY NOTES

14. ABSTRACT

This program aimed to fill the gap in photonic integrated circuit (PIC) capabilities by developing active wide-bandgap PIC platforms to operate from the ultraviolet to the infrared spectrum. We largely accomplished our goals, as detailed below, using III-nitride materials, most importantly aluminum nitride (AlN). Importantly, we designed and fabricated an AlN PIC platform that was then used for transformative experiments including multiphoton correlation spectroscopy with integrated superconducting nanowire detectors and large-scale hybrid integration of quantum "artificial atoms".

15. SUBJECT TERMS

Quantum Information, Photonic Integrated Circuits, Visible, Ultraviolet

16. SECURITY CLASSIFICATION OF:			17. LIMITATION OF ABSTRACT	18. NUMBER OF PAGES	19a. NAME OF RESPONSIBLE PERSON
a. REPORT	b. ABSTRACT	c. THIS PAGE			**KRISTI MEZZANO**
U	U	U	UU	57	19b. TELEPHONE NUMBER (*Include area code*) **N/A**

TABLE OF CONTENTS

LIST OF FIGURES

1.0 SUMMARY

This program aimed to fill a capabilities gap in photonic integrated circuits (PICs) by developing active wide-bandgap PIC platforms to operate from the ultraviolet to the infrared spectrum. We largely accomplished our goals, as detailed below, using III-nitride materials, most importantly aluminum nitride (AlN). Importantly, we designed and fabricated an AlN PIC platform that was then used for transformative experiments including multiphoton correlation spectroscopy with integrated superconducting nanowire detectors and large-scale hybrid integration of quantum "artificial atoms".

2.0 INTRODUCTION

PICs allow compact and stable integration of many optical components, including light sources, modulators, dispersive elements, beam splitters and combiners, as well as detectors. Indium phosphide (InP) PICs nowadays drive a large fraction of internet communications. Silicon PICs enable direct integration with complementary metal oxide semiconductor (CMOS) technology and are being deployed for optical interconnects, sensing, and a wide range of other applications. Both PIC material platforms are now available at semiconductor foundries, including through multi-project runs to distribute fabrication costs across a large set of end-users. However, these materials have a major limitation: they only transmit infrared light. This precludes a wide range of applications that require PICs in the visible or ultraviolet spectrum, including spectroscopy and biochemical sensing, beam steering and lidar, holography, certain types of communications, nonlinear optics, and quantum information processing (QIP). In the field of QIP alone, many applications would greatly benefit from a short-wavelength active PIC platform, including linear optics with room-temperature Si avalanche photodetectors (Si APDs) and interfacing with long-lived quantum memories -- neutral atoms, trapped ions, nitrogen vacancy (NV) centers in diamond, and other quantum emitters.

3.0 METHODS, ASSUMPTIONS, AND PROCEDURES

3.1 Methods and Procedures

The program rested from the outset on numerical modeling and theory of a PIC platform consisting of a crystalline $Al_xGa_{1-x}N$ optical guiding layer on an AlN substrate for the ultraviolet to visible (UV-vis) wavelength range[1]. Based on the above analysis[1], we developed a wide-bandgap photonics platform in AlN on sapphire.

Considered the ridge waveguiding structure shown in Fig. 1(a). The waveguide consists of an AlxGa1-xN ridge on a pedestal of AlN of height h on the AlN substrate. This pedestal reduces bending losses. The overcladding material, depending on the application, can be air or any other wide bandgap and transparent material such as water or SiO2 that have a refractive index lower than that of AlGaN. The AlxGa1-xN alloy has a bandgap from ~3.42 eV (~365 nm) for x = 0 to

~6.2 eV (~200 nm) for x = 1. To keep the lattice mismatch at the AlGaN/AlN interface below 1% and attain a large UV bandgap, we assumed x 0.65 as indicated in the pink region in Fig. 1(b). Though increasing the x reduces the refractive index difference between AlxGa1-xN and AlN, we showed that adequate optical mode confinement is available for the waveguides.

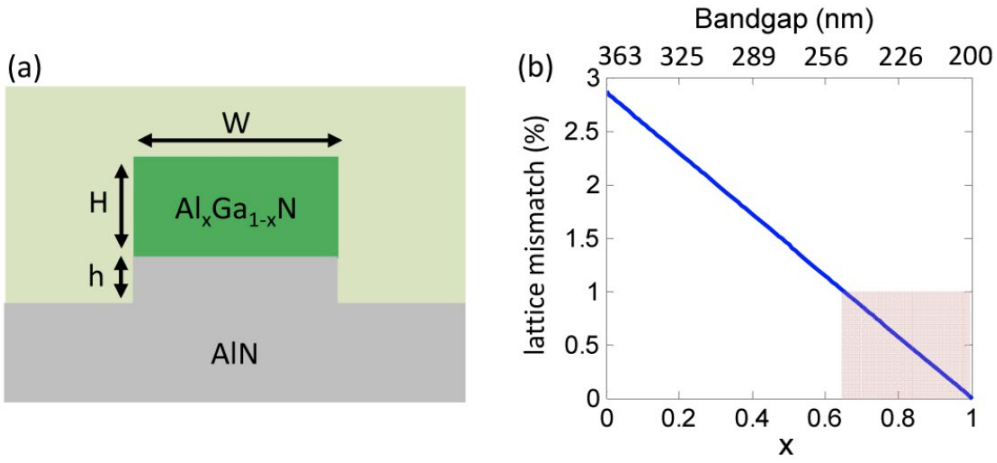

Figure 1: (a) cross section of the AlxGa1-xN waveguide discussed here. (b) Variation of AlxGa1-xN/AlN lattice-mismatch vs. x. The top horizontal axis shows the bandgap of AlxGa1-xN in the wavelength unit for each x value.

Fig. 2(a) and 2(b) show the refractive index difference for both ordinary (Δno) and extraordinary (Δne) directions between the AlxGa1-xN and AlN at four values of x>0.65. For x = 0.65, Δno ~0.090-0.12 and Δne ~0.090-0.14 over a wavelength range of 300 nm – 700 nm. The values of Δno and Δne approximately determine the guided-mode confinement for the transverse-electric (TE) and transverse-magnetic (TM) polarization modes, respectively.

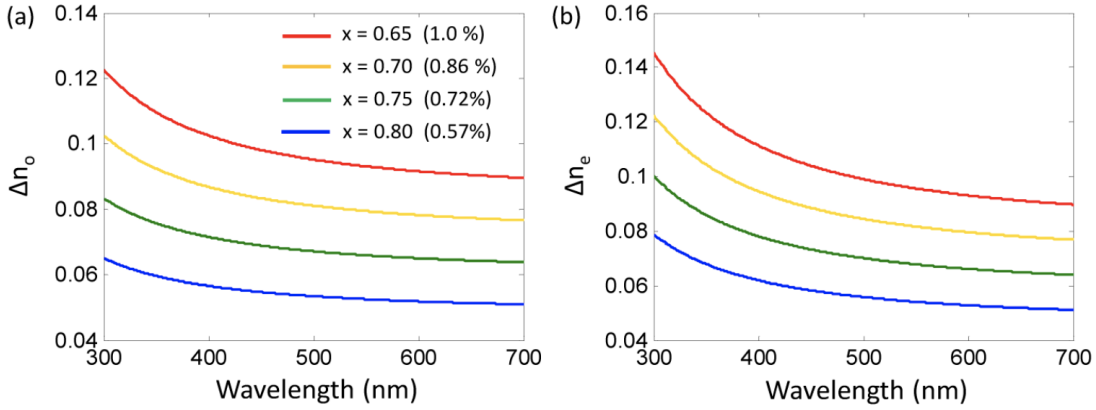

Figure 2: Plots of the Refractive Index Difference between the AlxGa1-xN and AlN for (a) ordinary and (b) extraordinary indices with the x values and lattice mismatches shown in the inset of (a).

Part of the promise of wide-bandgap photonics with nonlinear properties is the potential of photon-photon interactions mediated by a chi-2 medium. To this end, we studied the interaction between two photons in a nonlinear cavity[2,3] through numerical analysis of spontaneous mixing processes.

Figure 3(a) illustrates the commercially available AlN-on-Sapphire wafers from Kyma Technologies, Inc., consisting of 430 μm sapphire (Al2O3) with a 200 ± 10 nm c-plane AlN film on the top layer, which is used for fabricating PICs in this work. The c-plane AlN was grown on top of the sapphire substrate by pulsed DC magnetron sputtering, using a process called plasma vapor deposition of nanocolumns (PVDNC). This method produced an AlN thin film that is crystalline with the [0001] direction parallel to the growth direction. Atomic force microscopy of the AlN thin film shown in the inset of Figure. 3(a) indicates a flat surface with 0.9 nm RMS roughness. High-resolution X-ray diffraction (HRXRD) measurements in Figure. 3(b) indicate the high structural quality of the AlN thin film. The ω scan of (002) and (015) AlN peaks shows full-width-half-maximum (FWHM) of 0.12 degree and 0.20 degree respectively, while previous work of AlN thin films deposited on amorphous silica reported a FWHM of the XRD rocking curve to be less than 2 degrees with a 1 degree FWHM resolution limit in their system [24]. The single crystalline wurtzite structure across the wafer is evidenced by the (015) φ scan showing six-fold symmetry [Figure. 3(c)]. This flat surface and improved structural quality likely contribute to the low waveguide loss described below. Figure 1(d) plots the measured refractive index of the AlN film spanning from UV to VIS to near infrared wavelengths.

Figure 3(e) shows the power dependence of this platform's background autofluorescence using a scanning confocal microscope with a $\lambda = 532$ nm excitation pump laser (Coherent Verdi). A 0.95 numerical aperture (NA) microscope objective (Olympus UMPlanFl 100x) was used for the scanning confocal microscope, and a 532 nm notch filter as well as a 550 nm long-pass filter were used to filter out the 532 nm excitation pump in the fluorescence collection path. The photoluminescence (PL) was then fiber-coupled from free-space to a single-mode fiber via a 0.4 NA microscope objective (Olympus MA 20). The fiber-collected PL signal was either detected using single-photon avalanche photodiodes (Excelitas) or spectrally resolved on a grating spectrometer (Princeton Instruments, Acton SP2500i). We used the 4 μm diameter fiber facet as the pinhole for confocal imaging. Since the size of this fiber facet was not matched perfectly to the spot size at the sample plane, we collected a portion of the out-of-focus light. As such, when we measured the AlN autofluorescence, we were also pumping the underlying sapphire that is out-of-focus and collecting a portion of the sapphire PL. This claim is supported by the fluorescence spectrum of the AlN, which is shown in the bottom inset spectrum of Fig. 3(e). The AlN fluorescence spectrum is identical to that of the sapphire (not shown), which is in agreement with the fluorescence spectrum of sapphire found in literature[4]. The narrow luminescence double peaks at around 695 nm correspond to the ruby luminescence from the $^2E \rightarrow 4A_2$ transitions of Cr^{3+} ions that are substitutional in the Al sublattice.

For comparison, Fig. 3(e) also shows the autofluorescence results of a SiN sample under the same excitation and collection conditions; the fluorescence spectrum of SiN is also shown in the top

inset of Fig. 3(e). The SiN sample has close to four times the amount of fluorescence intensity as AlN; however, the amount of autofluorescence is dependent on the SiN composition and method of deposition[5]. Furthermore, the PL from pumping the AlN is mainly from the underlying sapphire substrate. Spectrally, this sapphire fluorescence is concentrated in a narrow band sapphire Cr line at around 695 nm, which can be easily filtered out by a notch filter. This is more favorable for quantum applications compared to the broadband SiN PL from 620 nm to 780 nm, which overlaps spectrally to NV in diamond spectrum[6]. A low autofluorescence makes AlN promising for interfacing with atomic transitions of ions[7], neutral atoms[8], and atom-like defects in diamond[6]. Ultimately the maximum allowed background count highly depends on the applications and protocol of the experiment. As long as the background fluorescence is optically detuned from the optical transitions of the quantum system one is working with, sufficient filtering can be achieved to improve signal-to-noise ratio.

Initially after deposition, the SiON cladding (to be discussed later) exhibited some fluorescence comparable to SiN, but we found that the SiON fluorescence can be bleached away by optically pumping the material with the excitation laser, as shown in Figure. 3(f). This photobleaching method of the SiON top cladding did not have any effect on the AlN or SiN materials.

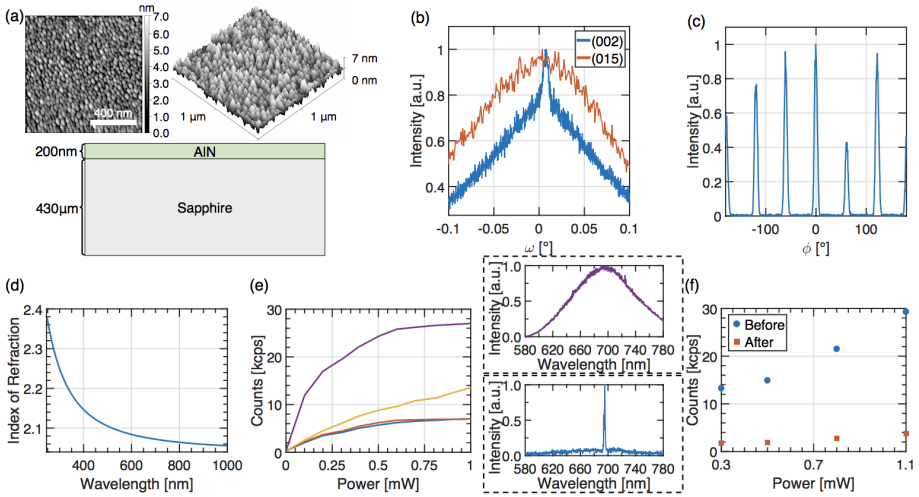

Figure 3: Properties of AlN-on-sapphire Material. (a) Cross section illustrating each layer of the wafer, along with their respective thickness; top inset: atomic force microscopy scan of AlN film showing the nanocolumn size. Surface roughness is measured to be 0.9 nm RMS with 26.5 nm grain size (b) High resolution x-ray diffraction (002) and (015) ω scan of AlN. (c) (015) φ scan of AlN showing six-fold symmetry wurtzite structure. (d) Refractive index measurements using ellipsometry. (e) Background fluorescence from sapphire substrate (yellow), unpatterned AlN (blue), patterned AlN (orange), and stoichiometric silicon nitride (purple). Top inset (purple): Fluorescence spectrum of SiN. Bottom inset (blue): Fluorescence spectrum of AlN. (f) Background fluorescence from SiON top cladding, before (blue circles) and after (orange squares) bleaching.

Figure 4(a) outlines the complete fabrication process. The process starts off with an unpatterned 1 cm × 1 cm AlN-on-sapphire chip diced from a whole wafer. Then, hydrogen silsesquioxane (2% XR-1541) is spun on after deposition of a 5 nm thick Cr discharge layer via electron beam evaporation. The hydrogen silsesquioxane (HSQ) film thickness was measured to be ~70 nm by using an AFM to measure the step feature profile after patterning. The patterns were written with an Elionix ELS-F125 electron beam lithography system at 125 kV. The patterns were developed using a salty developer, which is an aqueous mixture of 1 wt % NaOH and 4 wt % NaCl, for high contrast [29]. The AlN waveguides and photonic components were etched at an etch rate of 200 nm/min by inductively coupled plasma reactive-ion etching (ICP-RIE) using a gas mixture of BCl3/Cl2/Ar. We did not observe a significant change in the surface roughness from the etching, and a sidewall angle close to 90 degrees is achieved due to the combination of physical sputtering and plasma chemical etching. The BCl3/Cl2/Ar chemistry ICP-RIE etch did not result in any noticeable etching of the underlying sapphire substrate. Hence, the underlying sapphire acted as an etch stop layer in which we can overetch the AlN to ensure that it was completely cleared through without creating a sapphire ridge underneath the AlN waveguide structures. The Cr and HSQ were lastly removed with Cr etchant and buffered oxide etch (BOE), respectively. Figure 4(b) shows a scanning electron microscope (SEM) image of the fabricated AlN waveguide. Finally, the waveguides were clad with approximately 3 microns of SION using plasma-enhanced chemical vapor deposition (PECVD) or spin coated with approximately 2 microns of PMMA. In the case where the chip was cladded with SiON, the edges of the chip were mechanically polished back to the inverse-tapered waveguides for edge coupling.

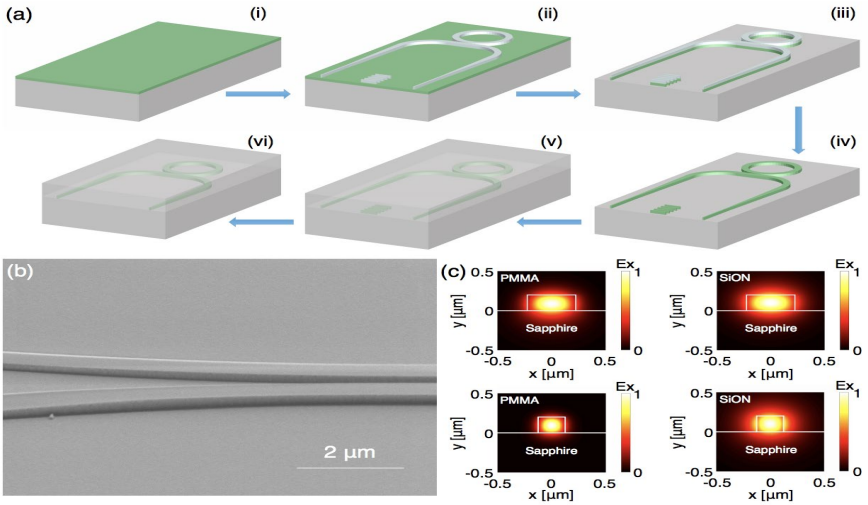

Figure 4: (a) AlN on sapphire photonics fabrication process: (i) Start off with an unpatterned AlN-on-sapphire chip diced up from a whole wafer. (ii) Spin coat HSQ (2% XR-1541), pattern using electron beam lithography, and develop using an aqueous mixture of 1 wt % NaOH and 4 wt % NaCl for high contrast. (iii) Etch by ICP-RIE using chlorine chemistry. (iv) Strip HSQ. (v) Clad with silicon oxynitride using plasma-enhanced chemical vapor deposition (PECVD). (vi) Edge polish for making the inverse-tapered edge couplers. (b) Scanning electron microscope (SEM) image of a fabricated AlN waveguide at a 50

degrees tilted view. (c) Transversal component of TE mode in AlN waveguide for PMMA and SiON cladding for 638 nm (top) and 400 nm (bottom) wavelengths. The dimensions of the waveguide for 638 nm wavelength are 450 nm wide × 200 nm thick. The dimensions of the waveguide for 400 nm wavelength are 250 nm wide × 200 nm thick.

The most popular methods for constructing a programmable mode transformer from N input to N output modes break the problem up into a mesh of 2 × 2 mode transformers consisting of Mach–Zehnder interferometers (MZIs)[9,10], as shown in Figures. 5(a) and 5(b). Each MZI consists of two 50% beam splitters and two phase shifters parameterized by (θ, ϕ), as shown to the right of Fig. 5(b). In integrated photonics platforms, beam splitters are commonly realized by directional couplers that convert input modes *a1, a2* into output modes b1, b2; note the $\pi/2$ phase in the cross terms guarantees unitarity of the directional coupler transformation. The MZI shown in the inset of Fig. 5(b) applies the SU(2) transformation, up to a global phase. Here we assumed the unit cell is lossless; accounting for losses requires each MZI to be described by a 4 × 4 matrix, rather than the 2 × 2 matrix considered here. Losses can be modeled by "virtual" beam splitters coupling the original mode and a "vacuum" mode. If such virtual beam splitters are included, the overall transformation can still be represented as a unitary UM, where M>N accounts for the additional loss channels. The N × N transformation that applies to our input and output waveguide modes then comprise a nonunitary submatrix of UM. In instances where the loss in each component is identical, it is possible to represent the PNP transformation by the unitary UN and to account for loss as a global parameter $\alpha \leq 1$ that can be factored out as $V(N) = \alpha U(N)$. Experimentally, waveguide losses have been shown to be relatively uniform, so that losses can likely be assumed to be uniformly distributed[11]. In this case, the scattering statistics for q identical, single photons passing through the PNP were described by UN, and the probabilities of all photons arriving at the output will scale as αq.

For a universal unitary transformation, each of the N input modes must be coupled to each of the N output modes. Figure 5(a) shows an arrangement of MZIs connecting N = 6 modes. To allow connections between all modes, one requires $\Sigma_n = N(N-1)/2$ (N choose 2) MZIs—15 MZIs for this example. The triangular arrangement of Fig. 5(a) was first proposed by Reck et al.[12]. Figure 5(b) shows a more compact arrangement, described by Clements et al.[13], that accomplishes the same UN transformation; it also requires 15 MZIs for N= 6 modes. Both the "Reck" and "Clements" decomposition algorithms terminate with a matrix that implements UN up to a diagonal phase screen. The phase screen can be implemented using phase shifters at each input mode, as shown in Figs. 5(a) and 5(b). A cascaded binary tree structure[14] that can implement arbitrary unitary transformations has also been proposed. The network shown in Fig. 5(c) was originally proposed by Miller as a method for realizing any linear transformation on a set of spatial modes[15]. This network uses a physical instantiation of the singular value decomposition, which is a factorization of any matrix (M) as $M = U\Sigma V^{\dagger}$, where U is an m × m unitary matrix; Σ is an m × n diagonal, rectangular matrix of nonnegative real numbers; and V is an n × n unitary matrix. Here, two universal unitary circuits (U, $V^{\dagger}$) are connected by a column of single MZIs that are used as variable attenuators implementing Σ. In the original implementation of the "Miller" network, each

MZI was implemented using two internal phase shifters with the differential phase between the two phase shifters being one parameter and the global phase imparted by the two phase shifters as another parameter[9,14,15]. The "Miller" MZI configuration can be more compact than the standard configuration, since the overall unit cell length is reduced by the length of one phase shifter

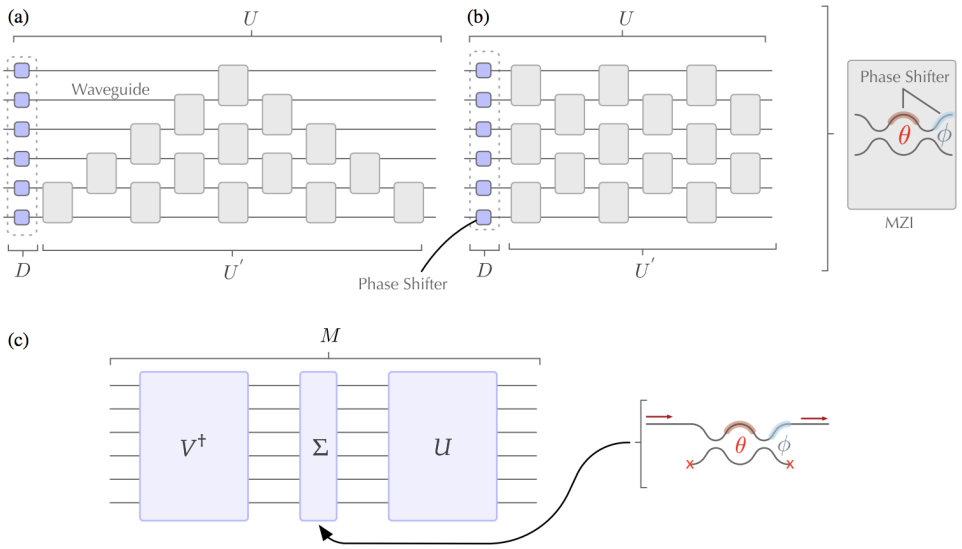

Figure 5: Universal Unitary Networks Composed of MZIs; (a) shows the "Reck" encoding and (b) shows the "Clements" encoding. Inset shows the unit cell of a PNP, a programmable MZI. (c) Universal linear network composed of two universal unitary circuits and an additional column of "loss" MZIs originally described by Miller [16].

A third application of wide-bandgap PICs is in quantum information processing. This direction followed from our earlier demonstration of hybrid integration of diamond qubits with silicon nitride[6], but with the advantage of AlN having far lower autofluorescence. Color centers in diamond have emerged as leading solid-state 'artificial atom' qubits because they enable on-demand remote entanglement, coherent control of over ten ancilla qubits with minute-long coherence times and memory-enhanced quantum communication. A critical next step is to integrate large numbers of artificial atoms with photonic architectures to enable large-scale quantum information processing systems. So far, these efforts have been stymied by qubit inhomogeneities, low device yield and complex device requirements. We therefore pursued a nanofabrication process for the high-yield heterogeneous integration of 'quantum microchiplets'—diamond waveguide arrays containing highly coherent colour centres—on a PIC[16].

Ion implantation: Figure. 6 summarizes the fabrication and integration processes. First, we relieved the strained surface of the single-crystal diamond plate (Element6) by plasma etching the first 10 μm of diamond in Ar/Cl2, followed by another 5 μm etching in pure oxygen plasma. We used an FIB51 tool at the Ion Beam Laboratory (Sandia National Laboratories) to implant Ge ions (spot size of about 35 nm × 43 nm) and Si ions (spot size of about 50 nm × 45 nm) at an effective areal dose of 2 × 1011–6 × 1011 ions per cm2 and 4.5 × 1011–9 × 1011 ions per cm2 , respectively. The Ge (Si) ion energy is 200 keV (170 keV), which corresponds to an implantation depth of 74 ± 12 nm (113 ± 19 nm) from stopping and range of ions in matter (SRIM) simulations52. After implantation, we annealed the devices at 1,200 °C in an ultrahigh vacuum furnace. Finally, we cleaned the diamond in a boiling mixture of 1:1:1 sulfuric acid, nitric acid and perchloric acid.

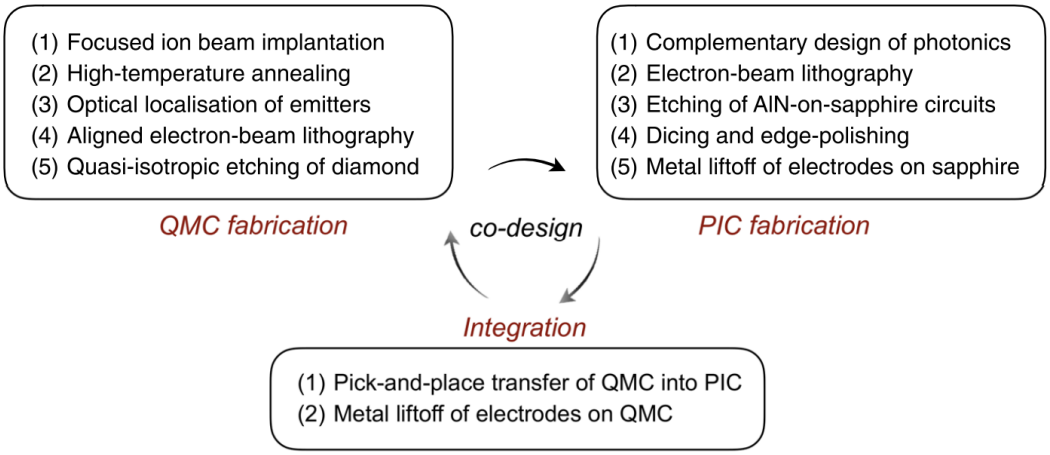

Figure 6: Flowchart for Large-scale Heterogeneous Integration.

Conversion yield of GeV and SiV centres: We analysed the conversion yields of GeV and SiV centres by counting the absence of fluorescent spots in our implantation region (1-μm pitch, square grid) using photoluminescence microscopy. A Poisson distribution P(k), with mean number of colour centres λ and number of observed emitters per spot k, models the stochastic emitter creation process. From the mean $\lambda = -\log(P(0))$ and our implantation dose, we estimate the conversion yield of GeV (SiV) centres to be about 1.9% (3.2%).

Yield of defect-free microchiplets: Using photoluminescence spectroscopy, we investigated the occurrence of defect-free 8-channel quantum microchiplets (QMCs), as summarized in Figure 7. From this histogram, we estimated the probability of creating defect-free QMCs to be 39%. We noted that this success probability depends on a variety of factors, including the alignment accuracy of the FIB implantation, the relative calibration between EBL and FIB, as well as the optical registration process. By deterministically placing each element of the QMC over pre-localized emitters, it should be possible to boost the yield towards unity, allowing hundreds or thousands of quantum channels per chiplet.

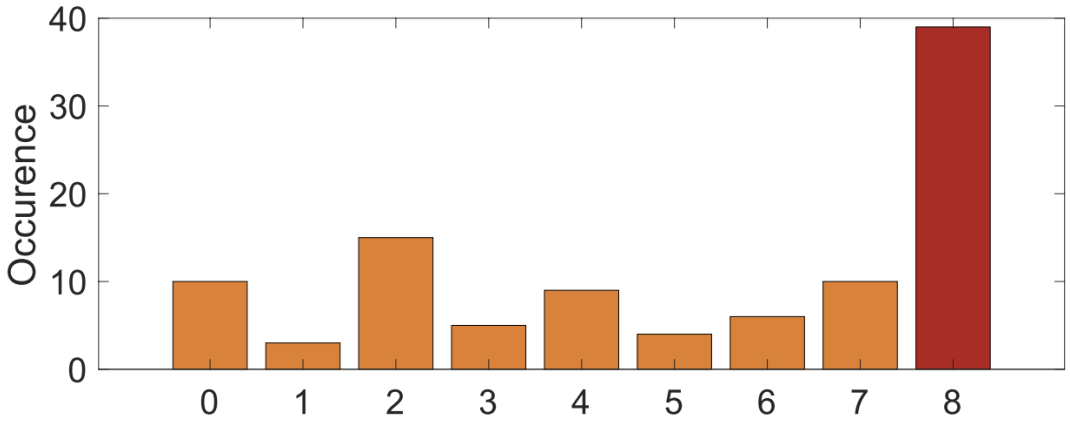

Figure 7: Histogram of Number of Emitter-coupled Waveguides within a QMC. The red coloured bar corresponds to the defect-free 8-channel QMCs that were suitable for integration. The orange coloured bars correspond to the QMCs that we did not use in this work.

Diamond–PIC coupling: Figure 8a, b show the normalized electric |E| field of 602-nm (737-nm)-wavelength transverse electric light coupling from the diamond waveguide (340 nm × 200 nm) to the bottom AlN waveguide (800 nm × 200 nm), calculated using the 3D FDTD method. The light transfers adiabatically via tapered sections in the diamond waveguide and AlN waveguide. Here the coupling region is 9 μm long, with a diamond taper length of 8 μm and AlN taper length of 5 μm. The top insets show 2D transverse cross-sections of the light propagation. The cross-sections at y = −10 μm and y = 1 μm correspond to the fundamental transverse electric mode of the diamond waveguide and AlN-on-sapphire waveguide, respectively. The cross section at y = −5 μm (y = −6 μm) is the point where half of the light launched from the diamond waveguide is transferred to the AlN waveguide at 602-nm (737-nm) wavelength. The light from the diamond waveguide couples to the AlN waveguide with 97% (98%) efficiency at these wavelengths, with all of the light coupling preferentially to the AlN fundamental transverse electric mode and negligible coupling to higher-order modes. This optimized device geometry was determined by optimizing for the coupling efficiency from the fundamental TE mode of the diamond waveguide to the fundamental transverse electric mode of the AlN while sweeping the diamond taper length, the AlN taper length, and the overlap region between the diamond and AlN waveguides. We showed a typical transverse placement error of 38 ± 16 nm for our transfer placement of the QMC to the microchiplet socket; in simulation, this displacement corresponds to a decrease of the coupling efficiency to 93% (89%) at 602-nm (737-nm) wavelength. Hence, we had a 0.46-dB tolerance in the coupling efficiency within our transfer placement accuracy. By directly measuring the PIC–diamond–PIC transmission efficiency, we found the interlayer coupling efficiency to be greater than 34%, which was lower than simulations probably due to scattering at the interfaces and the QMC cross-junctions.

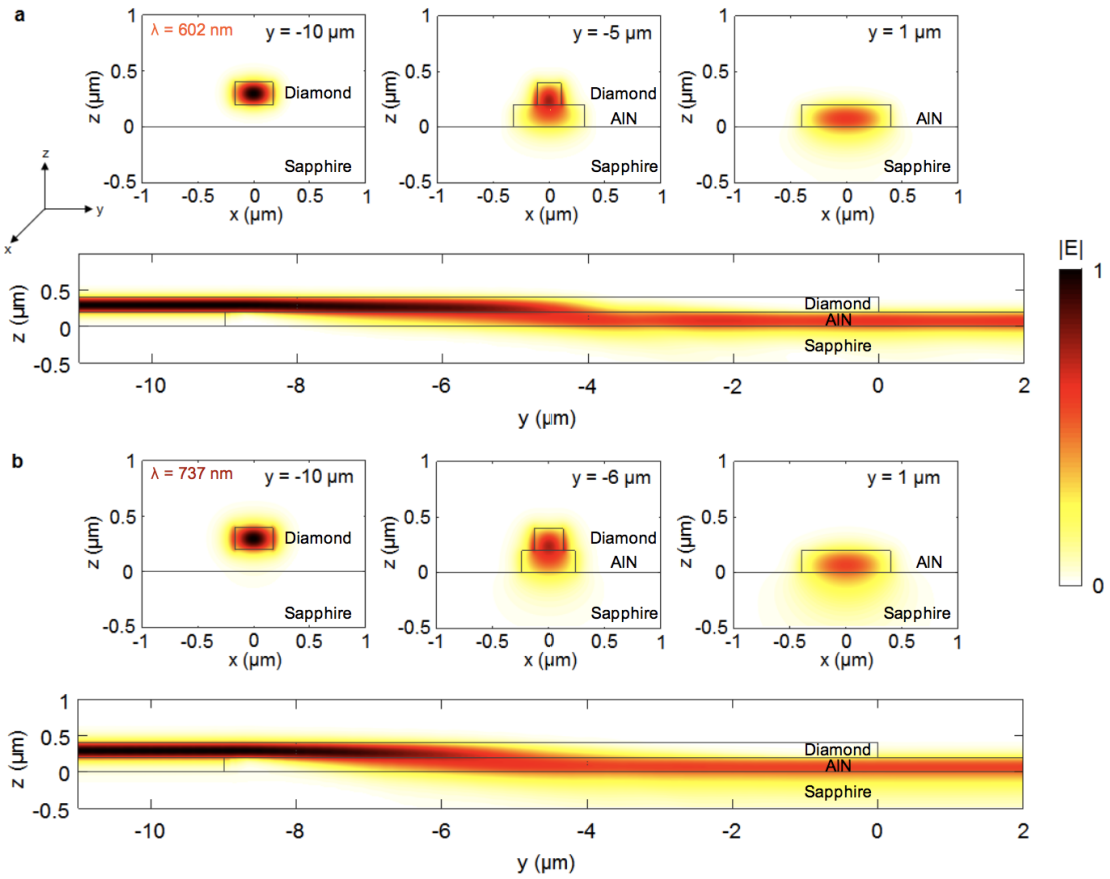

Figure 8:FDTD Simulation Showing Propagation of Light from the Diamond Waveguide into the AlN Waveguide. a, For a 602-nm wavelength (corresponding to the GeV colour centre ZPL). b, For a 737-nm wavelength (corresponding to the SiV colour centre ZPL).

PIC–fibre coupling: We coupled laser and photoluminescence to and from AlN-on-sapphire waveguides using lensed fibres (Nanonics Imaging, SM-630 with spot size 0.8 ± 0.3 μm and working distance 4 ± 1 μm) for cryostat experiments and ultrahigh NA fibres (UNHA3) for room-temperature experiments. Under our single-mode operation at 602–737 nm, the in-coupling efficiency is the same as the out-coupling efficiency of AlN waveguide to lensed fibre, which we found to be 51–57% using the 3D FDTD method. In practice, the PIC–fibre coupling efficiency, which we found to be about 11% in our devices, is sensitive to the edge coupler polishing quality. For the high-NA fibre, which is multimode at our wavelengths of interest, we found the numerical out-coupling efficiency to the fundamental fibre mode to be 25% (34%) at 602 nm (737 nm); there is also 1% (3%) coupling into higher-order modes.

System efficiency η: Figure. 9a shows the response from an idealized emitter system, fitted to $F = F_{sat}P/(P_{sat} + P) + cP$, where P is the continuous-wave 532-nm excitation pump power, cP is the linear background, Psat = 1.2 mW is the saturation power, F is the measured ZPL fluorescence at the detector and F_{sat} = 1.11 megacounts per second (Mcps). To independently measure the system efficiency at the detector, η_{system}, we used a pulsed source (SuperK Extreme, 532 ± 20 nm) with a

repetition rate of 26 MHz. From the saturation response (Fig. 9b), we determined F_{sat} = 0.25 Mcps and η_{system} = 0.72%. This experimentally determined efficiency is within a factor of five from the independently calculated $\eta system = 0.5\beta\eta_{PIC}\eta_{fibre}\,\eta_{setup} \approx 2.6\%$, where ($\beta$, η_{PIC}, η_{fibre}, η_{setup}) ≈ (0.55, 0.34, 0.33, 0.58) are the dipole-waveguide, diamond–PIC coupling, PIC–fibre coupling and external setup detection efficiencies, respectively. Here the factor of 0.5 accounts for the present configuration in which we collected the photon emission in one direction only. In these saturation experiments at room temperature, we used a lensed fibre with 2.5-μm spot size at 1,550 nm, which we found to have $\eta_{fibre} \approx 33\%$. We attributed the discrepancy to the non-unity radiative quantum efficiency of the emitter and deviations in β, η_{PIC} and η_{fibre} from independent measurements based on another device. In the next subsection, we outlined methods to improve the system efficiency.

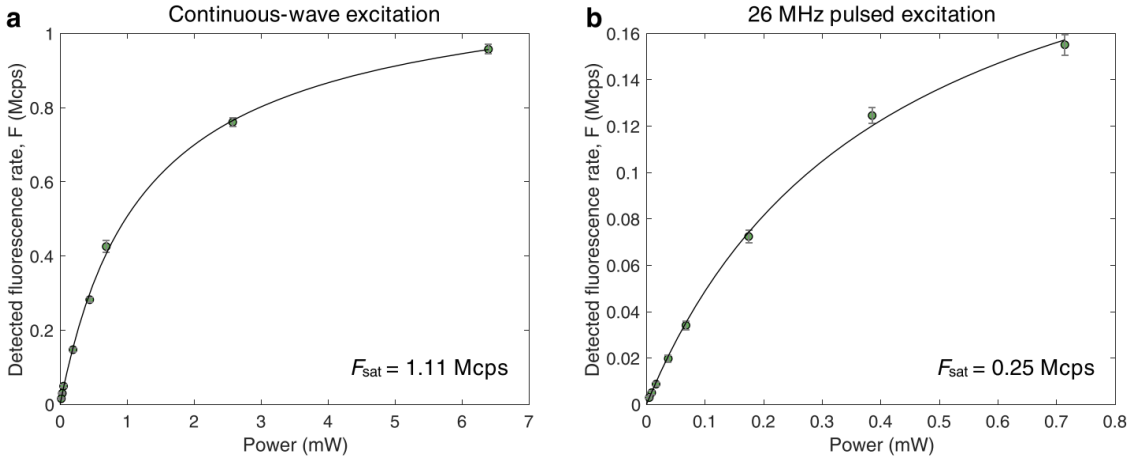

Figure 9: Saturation Response of a Single GeV Centre. a, Continuous-wave 532-nm laser excitation b, Pulsed laser excitation at 532 nm with a repetition rate of 26 MHz.

Strain tuning scheme of QMC on PIC: We introduced different optical responses to our emitter QMC by changing the length of their constituent waveguides. Here we used waveguides of length 20 μm (type I) and length 15 μm (type II). To be compatible with the QMC framework, we included a flexible bridge between type II waveguides and the QMC body (Figure. 9a). Figure. 9b confirms the difference in strain response at 30 V (modelled using COMSOL Multiphysics) between type I and type II waveguides.

We considered single GeV centres (emitter 1A, emitter 1B, emitter 2) indicated in Fig. 10a, Fig. 10 plots the spectral response of the optical transition lines up to an applied voltage of 30 V. From the increasing line splitting of the orbital ground states Δg, that is, between lines C and D (as well as A and B), we found that emitter 1B is a dipole whose axis lies in the transverse plane[17,18] of the waveguide. On the basis of the unidirectional shift of all four lines, emitters 1A and 2 are dipoles oriented in the longitudinal cross-sectional plane of the waveguide[17,18]. In particular, the global blueshift of the lines of emitter 1A indicates that it resides in a region with compressive strain (that is, below the neutral axis of the mechanical beam). Conversely, the optical lines of emitter 2 redshifts with applied voltage, indicating that it resides in a region with tensile strain, which is

located above the neutral axis of the waveguide. Figure. 11 shows the robustness of the strain-tuning mechanism as we repeatedly applied voltages from 10 V to 26 V. Above 30 V, we saw over 100 GHz of tuning of the two brightest transitions C and D for emitters 1A and 2; however, we note that in this regime there was hysteresis possibly due to stiction with the underlying gold and substrate about 150 nm and 200 nm away, respectively. Nevertheless, for the purpose here, we were able to spectrally overlap any pair of the three emitters with less than 25 V. Revised electrode, QMC and/or PIC designs in future microchips should be able to extend the spectral shift of individually tunable waveguides. We noted that the small 'pull in' voltage in our experiment appears earlier than it does in simulation (over 250 V)—possibly due to the surface conductivity of diamond[19,20]

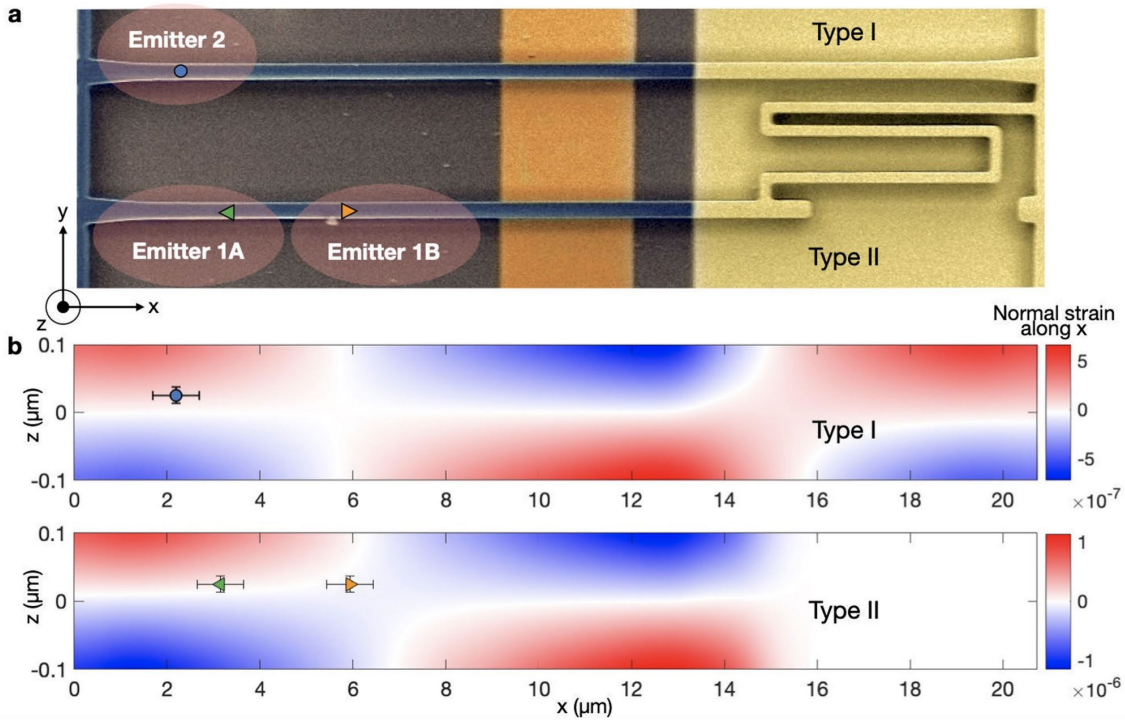

Figure 10: Scheme for Strain-tuning Emitters in a PIC Platform. a, SEM image of type I and type II waveguides considered in this experiment. b, Strain distribution along the waveguides and emitters. Horizontal error bars indicate the lateral uncertainty in the position of emitters and vertical error bars indicate the ion implantation straggle.

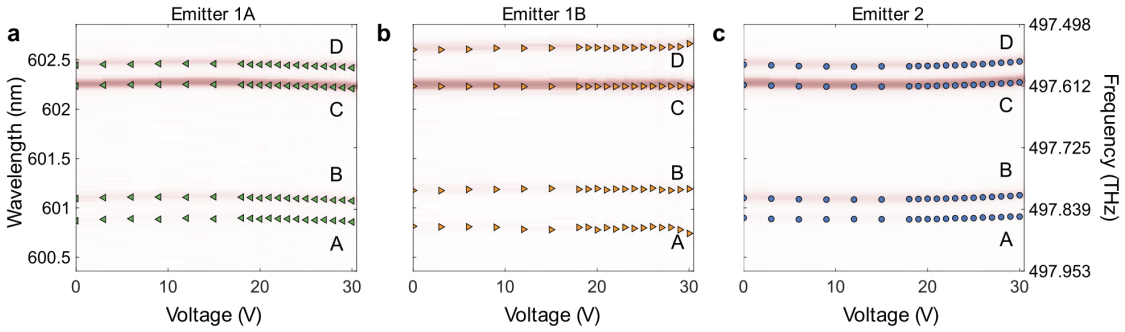

Figure 11: Spectral Shift of GeV Centres in Response to Strain Fields. a–c, Strain response of emitter 1A (a), emitter 1B (b) and emitter 2 (c).

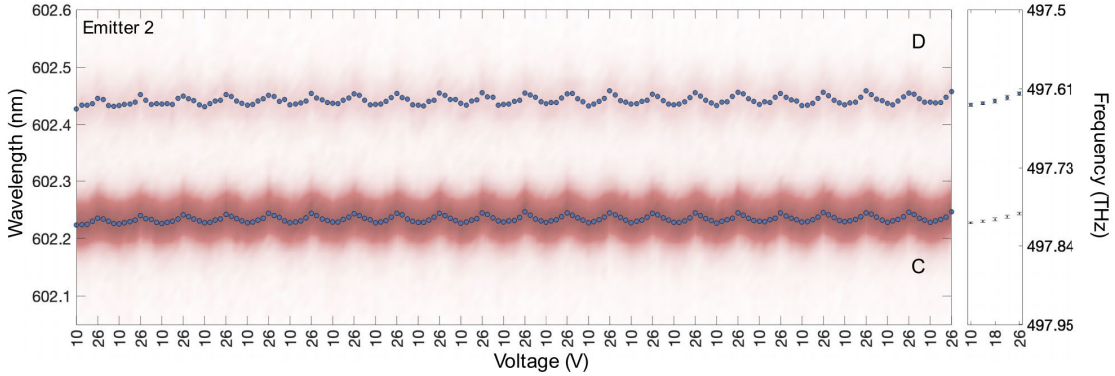

Figure 12: Spectral Shifts for the Brightest Transitions. Reproducible spectral shifts between 10 V and 26 V for the two brightest transitions C and D for emitter 2.

A final goal of this program was to investigate color centers in the AlN waveguide material itself. In particular, solid-state quantum emitters (QEs) are fundamental in photonic-based quantum information processing. There is strong interest to develop high-quality QEs in III-nitride semiconductors because of their sophisticated manufacturing driven by large and growing applications in optoelectronics, high voltage power transistors, and microwave amplifiers. As part of this program, we studied the generation and direct integration of as-grown QEs in an aluminum nitride-based PIC platform via optical photoluminescence spectroscopy.

4.0 RESULTS AND DISCUSSION

4.1 AlGaN/AlN integrated photonics platform for the ultraviolet and visible spectral range

An Al composition of x~0.65 provides a refractive index difference of ~0.1 between AlxGa1-xN and AlN, a small lattice mismatch (< 1%) that minimizes crystal dislocations at the AlxGa1-xN/AlN interface. This small refractive index difference is beneficial at shorter wavelengths to avoid extra-small waveguide dimensions. The platform enables compact waveguides and bends with high field confinement in the wavelength range from 700 nm down to 300 nm (and potentially

lower) with waveguide cross-section dimensions comparable to those used for telecom PICs such as silicon and silicon nitride waveguides, allowing for well-established optical lithography.

For the simulation of the modes of the waveguide shown in Fig. 1(a) we chose the popular aspect ratio of W = 2.5 H and consider two cases of h = 0 and h = H/2. We chose SiO2 as the overcladding for the simulation. The results would not change much if we had selected air or water overcladding because the refractive index of these three materials are much smaller than that of AlGaN, and so the waveguiding condition is mainly governed by the AlGaN/AlN refractive index difference. Fig. 13 shows the guide-mode cut-offs for different waveguide dimensions and AlGaN material compositions. This platform can potentially enable cost-effective, manufacturable, monolithic UV-vis photonic integrated circuits. Figures 13(a) and 13(b) show a map of the simulated TE and TM modes for an Al0.65Ga0.35N waveguide. A broad optical spectrum from 300 to 700 nm is guided by varying the waveguide W and H. The regions of single-mode, multi-mode, and mode cut-off are given in Fig. 13(a) and 13(b). The colormaps represent the power confinement factor in the core of the waveguide. From these figures we saw that single mode propagation and strong mode confinement were possible for Δn ~0.1 (for x = 0.65, see Fig. 2). The TE polarization [Fig. 13(a)] is guided over a narrower wavelength range than the TM polarization [Fig. 13(b)] because of a smaller in-plane refractive index difference Δno than the out-of-plane refractive index difference Δne. The insets in Fig. 13(a) and 13(b) show the optical power-density mode profiles, corresponding to the point marked by the star in Fig. 13(a) and 13(b).

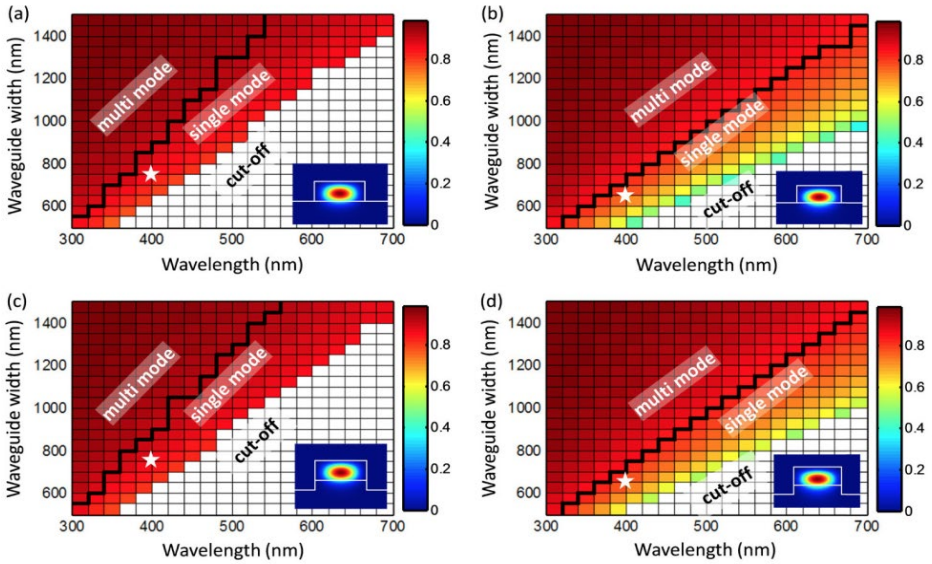

Figure 13: Simulated Guided-mode Map for an $Al_{0.65}Ga_{0.35}N$ Waveguide When W = 2.5 H and for the Following Cases: (a) TE polarization, h = 0, (b) TM polarization, h = 0, (c) TE polarization, h = H/2, (d) TM polarization, h = H/2. In each figure, the colormap represents the power confinement factor in the core of the waveguide. The regions of single-mode, multi-mode, and cut-off have been highlighted. The colorbars for each figure correspond to the colormap data. The insets in a-d show the waveguide mode intensity profile corresponding to the white star marker in the guided-mode map.

We repeated the waveguide analysis for a finite-thickness pedestal (h>0). Figures 13(c) and 13(d) again show broadband waveguiding, for the TE and TM polarizations, respectively and for h = H/2. The guided modes are similar for h = 0 and h = H/2 as seen from the results in Fig. 13, but the finite pedestal thickness reduces radiation in waveguide bends. We repeated these simulations for $Al_{0.75}Ga_{0.25}N$ waveguides under the TE and TM, W = 2.5H, and h = 0 or H/2 constraints (not shown). Simulations for x = 0.65 and x = 0.75 provide a straight-line approximation to the single-mode condition as $W = \alpha\lambda + \beta$ (where λ is the wavelength and α and β are constants) that allows direct comparison of W(single-mode) vs. λ. Figure 14 plots these lines that delineate single-mode conditions of AlGaN waveguides in the UV-vis range.

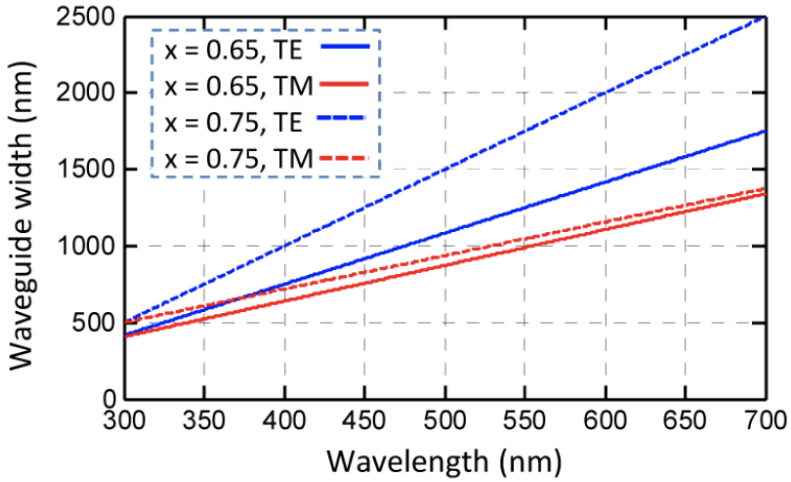

Figure 14: A straight line approximation showing the single-mode condition for TE and TM polarization modes of an AlxGa1-xN waveguide for x = 0.65 and 0.75, and for the case of h = 0, and W = 2.5 H. The single-mode condition in these plots corresponds to a mode confinement factor close or above 80%. The h = H/2 results are not shown as they are close to those of h = 0.

To show that a small refractive index difference between AlGaN and AlN is very beneficial for waveguide design at shorter wavelength, we simulated the guided modes at a UV wavelength of 300 nm for various waveguide heights (H) and widths (W). Figure 15(a) and 15(b) show the results for the TE and TM polarizations respectively. From these results and for a single mode condition, the waveguide dimensions are comparable to those used for Si waveguide at telecom wavelengths, thereby, the lithography of these UV waveguides is possible with existing photolithography technology.

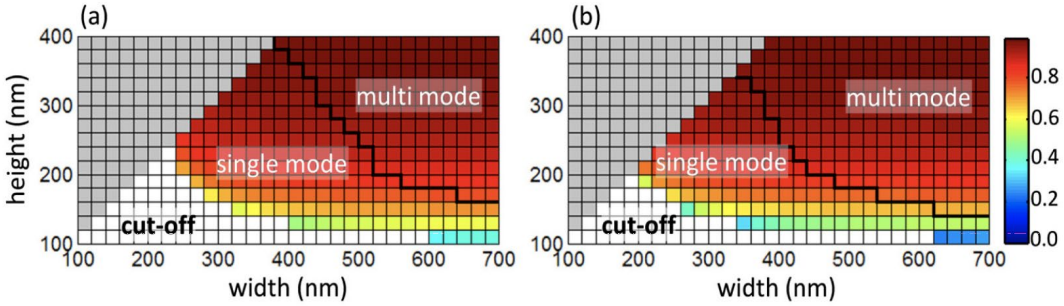

Figure 15: Simulated Guided-mode Map for an $Al_{0.65}Ga_{0.35}N$ Waveguide for Different Heights (H) and Widths (W) and a Pedestal h = 0, at a Wavelength of 300 nm for (a) TE and (b) TM polarizations. The colormap represents the power confinement factor in the core of the waveguide. The regions of single-mode, multi-mode, and cut-off have been highlighted. For each waveguide height, the waveguide width varies from that height value to 700 nm; therefore, the gray region is excluded in our analysis.

The passive waveguides considered thus far could be modified for electro-optical modulation through the Pockels effect or carrier injection/depletion[21]. The Pockels coefficient of AlGaN is expected to be close to that of AlN (~1 pm/V), though it may be increased by strain engineering. A reverse-biased PIN diode across intrinsic AlGaN would induce Franz-Keldysh electro-absorption modulation at photon energies ~50 meV below the band edge[22].

To analyze bending losses, we simulated optical resonances of circular $Al_{0.65}Ga_{0.35}N$ microring resonators on an AlN substrate and found their radiation-limited quality factor (Qr). The simulations are for TE-like modes near a wavelength of 300 nm. We find Qr using the relation $Qr = \omega r/(2\omega i)$ where ωr and ωi are the real and imaginary part of the resonance, respectively.

Figure 16(a) plots the simulated Qr for two pedestal thicknesses of h = 0 and h = H/2. The results in Fig. 16(a) show that compact resonators with high Q factors can be obtained for a small refractive index difference between Al0.65Ga0.35N and AlN (see Fig. 2 for the refractive index data). For h = H/2, Qr is consistently higher and permits high Q factors for radii below 5 μm. Figures 16(b) and 16(c) show the cross section mode profiles for the electric field in the radial direction for a radius of 15 microns and for two cases of h = H/2 and h = 0, respectively. Figure 16(d) shows the roundtrip bending loss of the resonators simulated in Fig. 16(a). The roundtrip loss in dB scale is $10\log_{10}(e^{-\alpha 2\pi R})$ where R is the radius and α is the propagation loss per unit of length, and is related to Qr as $\alpha = 2\pi n_g/(\lambda Qr)$, where λ is the wavelength and ng is the group index of the optical mode.

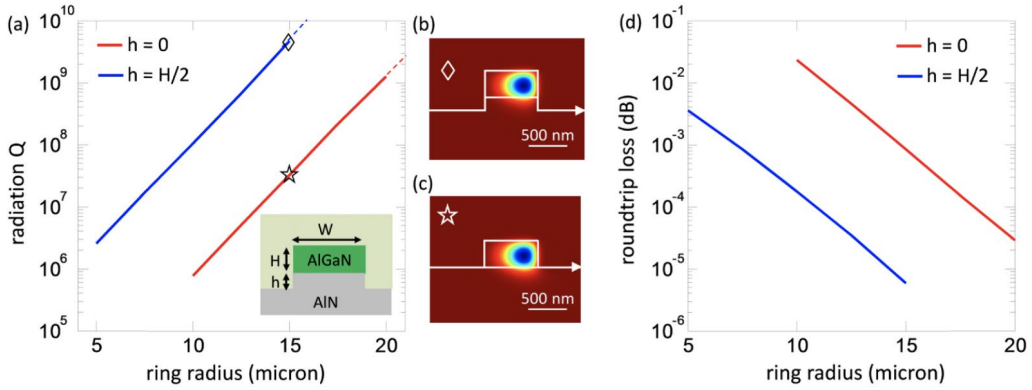

Figure 16: (a) Simulated radiation Q for the TE mode of an Al0.65Ga0.35N ring resonator vs. its radius for a resonance wavelength ~300 nm and for h = 0 and h = H/2. The inset shows the ring cross section. For this simulation W = 700 nm, H = 350 nm. (b)-(c) Cross section of the radial electric field mode profiles for a ring radius of 15 microns for h = H/2 and h = 0, respectively. (d) Roundtrip loss of the rings in (a).

C-axis AlN wafers were cut from a wurtzite single-crystal AlN boule grown by proprietary methods[23,24], and their UV transparency depended upon the crystal quality. The largest AlN boules grown to date have 50 mm diameter, and 32 mm diameter is available commercially. A challenge was to reduce the crystalline dislocation density in AlN. State-of-the-art single crystal growth of AlN produces dislocation densities below 1000/cm2 , and selected areas can have <100 defects/cm2. In the present art, AlN wafers show an absorption of less than 15 cm−1 over the 230 to 700 nm wavelength range, and less than 8 cm−1 for the 510 to 700 nm wavelengths[23]. These optical absorption results are promising and can be further improved by advancing the crystal growth techniques. A possible approach to further reduce dislocations near the AlGaN waveguide layer is to epitaxially grow a buffer layer of AlN on this AlN wafer before growing AlGaN. A near-term approach for large-scale wafers of AlGaN films is to use substrates of SiC, Si[25], or sapphire[26] with an optically thick, epitaxially grown spacer layer of AlN. Figure 17(a) shows a waveguiding structure in this platform. The lattice mismatch between the AlN and these aforementioned substrates determines the dislocation density at the lower AlN surface. Figure 17(b) summarizes the lattice mismatch between AlN and the potential growth substrates. With recent advances in growth techniques[27], the growth of an AlN spacer layer with minimal dislocation density on these substrates is possible.

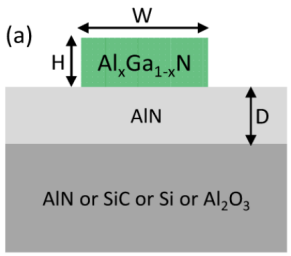

(b)

material	AlN	SiC	Si (111)	GaN	Sapphire
lattice constant (A°)	3.1106	3.081	3.84	3.189	4.758
lattice mismatch to AlN	0%	0.94%	19%	2.47%	13.3%*
thermal expansion coeff. ($\times 10^{-6}$ K^{-1})	5.27	4.3	2.6	3.17	5

*: Growth of AlN on sapphire includes a 30 degree rotation of the AlN growth plane (a-axis) around the growth direction (c-axis) resulting in a lattice mismatch of 13.3%.

Figure 17: (a) AlGaN-on-AlN waveguide structure on a substrate that can be AlN, SiC, Si or Al_2O_3. The thickness D is large enough (e.g. 2-3 µm) to avoid the leaking of the optical mode to the underneath substrate if not AlN. (b) Lattice parameters and temperature expansion of crystal wafers upon which AlN has been epitaxially grown.

4.2 An Aluminum Nitride Integrated Photonics Platform for the Ultraviolet to Visible Spectrum

The photonics platform guides light at low loss from the ultraviolet (UV) to the visible spectrum. We measure ring resonators with intrinsic quality factor (Q) exceeding 170,000 at 638 nm and Q >20,000 down to 369.5 nm, which shows a promising path for low-loss integrated photonics in UV and visible spectrum. This close collaboration with AFRL resulted in a joint publication in which MIT PhD student Tsung-Ju Lu and RIT PhD student Michael Fanto are equal lead authors[28].

Figure 18 highlights two methods to couple light into and from the PIC: grating couplers and inverse-tapered edge couplers. Due to the narrow frequency response of grating couplers, two different grating couplers were used for testing components in the visible wavelength from 500 nm to 700 nm wavelength: a green wavelength grating coupler optimized for 500 nm to 600 nm [shown in the top SEM image of Fig. 18(a)] and a red wavelength grating coupler optimized for 600 nm to 700 nm [shown in the bottom SEM image of Fig. 18(a). Figures 18(b) and 18(c) show comparisons between the simulated coupling efficiency spectra and the experimentally measured transmission spectra for the green and red wavelength grating couplers, respectively. The general shape of the experimental grating coupler transmission spectra matches well with the simulated coupling efficiency spectra. The experimental coupling efficiencies are listed in arbitrary units because we did not experimentally mode-match the spatial modes of the grating coupler and collection objective. The peak experimental transmission intensity for the green wavelength grating coupler is 0.1544 [a.u.] at 532.9 nm, while the peak experimental transmission intensity for the red wavelength grating coupler is 0.1565 [a.u.] at 625.3 nm.

Both green and red wavelength grating couplers are optimized for TE polarization, so the simulated coupling efficiencies model the collection of TE polarized light injected into the 450 nm wide by 200 nm tall AlN waveguide on bulk sapphire and scattered by the grating coupler. For the green wavelength grating coupler, the first gap width is 60 nm and the first grating period is 285 nm. Then, the gap width and grating period both linearly increase from 101 nm and 325 nm to 150 nm and 346 nm, respectively (increasing linearly in each period for 17 periods). Finally, the gratings

maintain a gap width of 150 nm and grating period of 346 nm for the remaining 9 periods. In a similar fashion, for the red wavelength grating coupler, the first gap width is 60 nm and the first grating period is 285 nm. Then, the gap width and grating period both linearly increase from 101 nm and 401 nm to 132 nm and 414 nm, respectively (increasing in each period for 10 periods). Finally, the gratings maintain a gap width of 132 nm and grating period of 414 nm for the remaining 10 periods. For both the green and red wavelength grating couplers, the dimensions of each individual grating period are optimized in order for the spatial mode profile of the diffracted light to be a Gaussian field profile. The grating couplers are also designed to be cladded with PMMA, rather than simple air cladding, in order to increase the out-of-plane coupling efficiency by pulling more of the optical mode away from the underlying sapphire substrate as PMMA has a higher refractive index than air. Both grating couplers are designed for an etch depth of 200 nm in order for ease of fabrication so that the grating couplers and waveguides can be fabricated in the same steps with no additional processing. Therefore, we believe grating couplers with even higher collection efficiency can be achieved with partially etched gratings. All measurements done in the VIS wavelength range of 500 nm to 700 nm use grating couplers for coupling light into and out of the chip.

Next, the fiber edge coupling is shown in Fig. 18(d), with UV fiber (Nufern SM300) and an excitation wavelength of 369.5 nm. Figures 18(e) and 18(f) show free-space edge coupling using aspheric lenses into waveguides that are designed to be single mode in the traverse electric polarization at 468 and 369.5 nm, respectively. The inverse-tapered waveguides adiabatically transform and expand the AlN waveguide mode to the fiber waveguide mode at the chip's edge facet. As such, for the inverse-tapered edge couplers, a SiON cladding is used in order for the refractive indices of the materials surrounding the AlN waveguide to be to be uniform such that the AlN waveguide mode can be expanded in a circularly symmetric way in order to match to the Gaussian mode of a fiber at the chip's edge facet. All measurements done in the UV wavelength range of 360 nm to 480 nm use edge couplers for coupling light into and out of the chip. It is difficult to quantify the experimental edge coupling loss based on the sources of loss we have. In measuring the transmission loss of sending light into the input edge coupler facet and collecting from the output edge coupler facet, the light propagates along a waveguide that spans across multiple electron beam lithography write fields. At each write field boundary, a dislocation of the waveguide due to stitching errors result in scattering points that contribute to the overall facet-to-facet transmission loss. As such, measuring the transmission loss is not an accurate estimation for the edge coupler coupling loss. However, we are able to achieve at least 40% transmission from input edge facet to output edge facet in our devices.

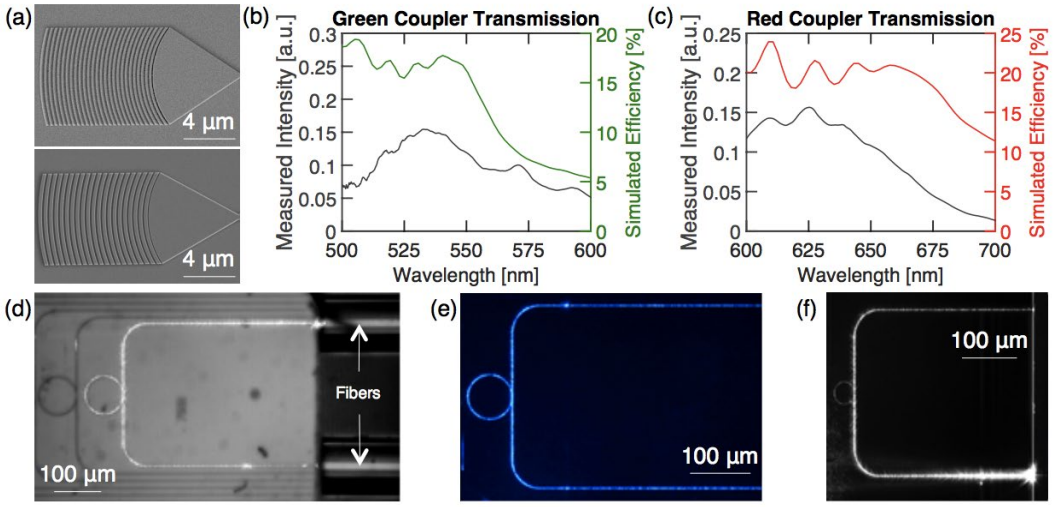

Figure 18: (a) SEM images of the grating couplers. First gap of the grating coupler is 60 nm, and the gaps are linearly increasing. Curvatures are set to be matched with mode evolution so that there is no reflection. Top: green spectrum grating coupler. Bottom: red spectrum grating coupler (b) Green line: simulated coupling efficiency vs. wavelength plot of green-spectrum grating coupler optimized for 500 to 600 nm. Black line: measured experimental transmission intensity vs. wavelength plot of green-spectrum grating coupler. (c) Red line: simulated coupling efficiency vs. wavelength plot of red-spectrum grating coupler optimized for 600 to 700 nm. Black line: measured experimental transmission intensity vs. wavelength plot of red-spectrum grating coupler. (d) Fiber edge coupling to the waveguides at 369.5 nm using Nufern SM300 fiber. (e), (f) Free-space edge coupling using aspheric lenses into waveguides that are designed to be single mode in the transverse electric polarization at 468 nm and 369.5 nm, respectively.

Figure 4(c) shows simulated electric field profiles of the AlN waveguide modes for PMMA and SiON cladding for 400 nm and 638 nm wavelengths. The waveguides support a single transverse electric (TE) mode for their respective wavelengths. Wrapping these waveguides into rings produces the high Q resonators. The ring resonator measurements are summarized in Fig.19. Figure 19(b) shows the response at 369.5 nm of the 40 µm radius ring resonator cladded with SiON around resonance; a Lorentzian fit indicates a Q of >24,000. The resonance in the ring was measured by mapping the intensity of the light scattering from the ring by means of a UV sensitive camera placed in a microscope above the device. After measuring several devices with increasingly larger waveguide-ring gaps and finding the coupling of the waveguide to the ring decreases each time without transitioning from overcoupled regime to critically coupled regime to undercoupled regime (or at least just from the critically coupled regime to undercoupled regime), we found the smallest waveguide-ring gap resonator to be undercoupled. Since the resonator is undercoupled, the ring resonance cannot be measured directly through an access bus waveguide. Hence, the data shows a resonance peak rather than a dip. Figure 19(c) shows the quality factors of various 40 µm radius ring resonators measured using an optical spectrum analyzer (OSA) for various sampled resonance wavelengths spanning from 380 nm to 480 nm, along with the quality

factors at around 369.5 nm using both a frequency doubled pulsed Ti:Sapphire laser (Spectra-Physics Mai Tai) and a continuous-wave (CW) tunable Ti:Sapphire laser (M Squared SolsTiS). The spacings between the sets of sampled wavelengths are not indicative of the ring resonator's Free-Spectral-Range (FSR). Rather, the Free-Spectral-Ranges of the various 40 µm radius ring resonators that we measured from 360 nm to 480 nm span from 0.22 nm to 0.4 nm. If we assumed that the propagation loss is dominated by the sidewall scattering loss and linear absorption loss of the material, then we can estimate the propagation loss using the equations for calculating the loss rate α given the resonator Q.

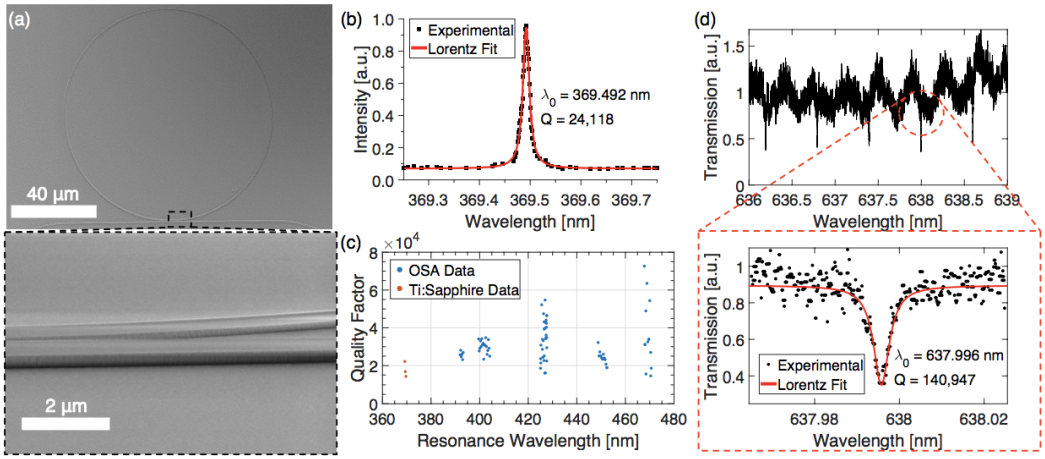

Figure 19: (a) SEM of the ring resonator. Inset shows a close up of the ring resonator at a 50 degrees tilted view. The gap between the waveguide and the ring is 300 nm for the undercoupling regime, which was used to verify the unloaded Q. (b) Wavelength response at 369.5 nm of the ring resonator cladded with SiON around resonance. The Lorentzian fitting shows a Q of >24,000. (c) Quality factors of 40 µm radius ring resonators measured using an optical spectrum analyzer (OSA) for wavelengths spanning from 380 nm to 480 nm, along with the quality factors at 369.5 nm wavelength using both frequency doubled pulsed and continuous-wave (CW) TI:Sapphire lasers. (d) Wavelength response at 637 nm of the ring resonator cladded with PMMA around resonance. The Lorentzian fitting shows a Q of >140,000. Inset shows a zoom-in of the wavelength response.

Distributed Bragg reflectors (DBRs) represent another important PIC component as broadband on-chip reflectors and filters. To further support this point, we developed a distributed Bragg reflector with high extinction for 532 nm for use as on-chip filtering of the excitation pump light used for exciting NV centers in diamond. The DBR has a period of 140 nm with 50% duty cycle, and it was designed to have an adiabatic tapering from the regular waveguide into the DBR in order to have low insertion loss. Also, the DBR was designed to structurally have rounded features for ease of fabrication. Figure 20(a) shows an SEM image of the fabricated DBR. The overlay blue plot in Fig. 20(b) shows the simulated transmission spectrum for the DBR, which has 45 dB extinction for the 532 nm green pump light. The black plot in Fig. 20(b) shows at least 13 dB extinction

experimentally for the DBR. We expected the extinction to be even higher because the attenuated 532 nm signal was at the noise floor of our experimental system.

The decreased transmission of the DBR simulation at wavelengths around 500 nm is due to the third order TE mode at around 500 nm wavelength for the ~735 nm wide waveguide portions of the DBR. At the wider sections of the DBR, the first order TE mode can couple with this mode, which is leaky since it cannot propagate through the entirety of the DBR due to the fact that the third order TE mode is not allowed at the narrower sections of the DBR.

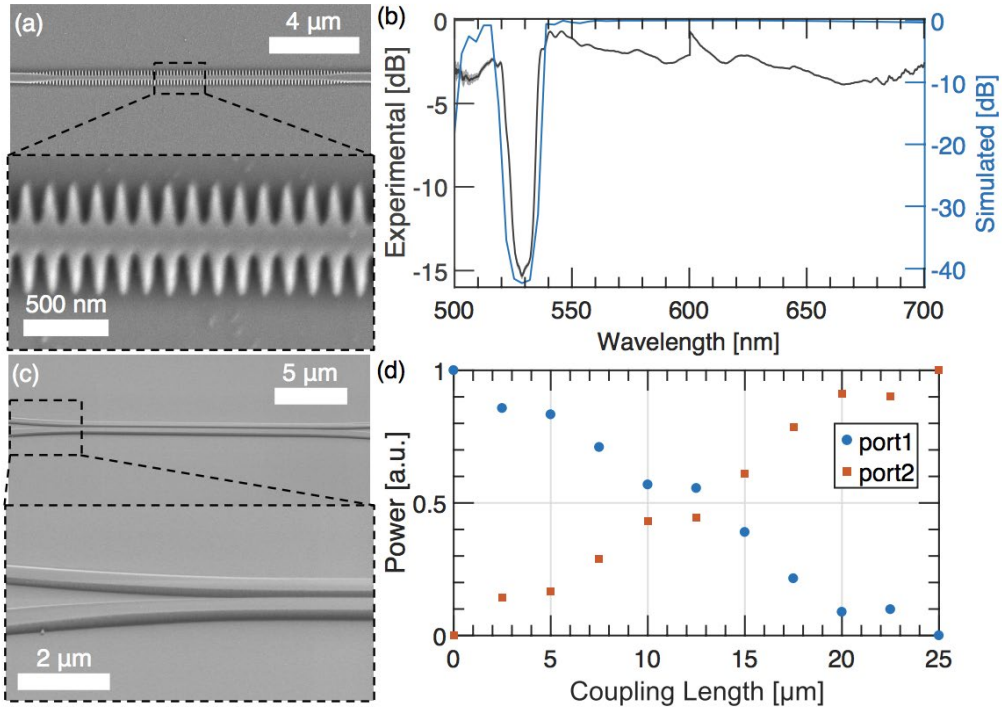

Figure 20: (a) SEM of the distributed Bragg reflector (DBR) with adiabatic tapering for low insertion loss. Inset shows a zoom-in of the DBR. (b) Simulated and measured transmission vs. wavelength for the DBR. In simulation, we achieve 45 dB extinction for 532 nm green pump light typically used for NV excitation. Experimentally, we achieve >13 dB extinction for 532 nm. (c) SEM of directional couplers with 50/50 splitting ratio at a 50 degrees tilted view. Inset shows a zoom-in of the directional couplers at a 50 degrees tilted view. (d) Measured transmission power at the two output ports of the directional couplers as a function of coupling length in the straight, parallel waveguides region.

Moreover, in collaboration with Prof. Karl Berggren, we used the AlN-Sapphire architecture to develop a scalable multi-photon coincidence detector based on superconducting nanowires. This work was published in Nature Nanotechnology in 2018[29] and now allows single photon detection across large waveguide circuits.

4.3 Linear programmable nanophotonic processors

As part of this program, we also wrote a review paper with our collaborators at AFRL (Rome, NY)[30]. Advances in photonic integrated circuits have recently enabled electrically reconfigurable optical systems that can implement universal linear optics transformations on spatial mode sets. This review paper covers progress in such "programmable nanophotonic processors"(PNPs) as well as emerging applications of the technology to problems including classical and quantum information processing and machine learning. PNPs have been demonstrated in a number of material platforms, some of which are summarized in Figure 21.

The SOI platform offers an especially high index contrast of 3.4:1.5, which enables low-loss waveguide bends with radii as small as 2 μm[31]. The resulting high component densities are especially important for large PNPs, which already can have up to 88 MZIs connecting 26 optical modes, as shown in Fig. 21(a), and applications are demanding much larger devices. Figure 21(b) shows a silicon photonics-based U4 PNP that was used for separating a multimode channel into individual single-mode waveguides. The U6 PNP was realized in germanium-doped glass with thermal modulators, illustrated in Fig. 20(c), and enabled the demonstration of linear optical quantum gates and boson sampling schemes[10]. Figure 20(d) shows a silicon photonics-based U4 PNP used to demonstrate a universal coupler.

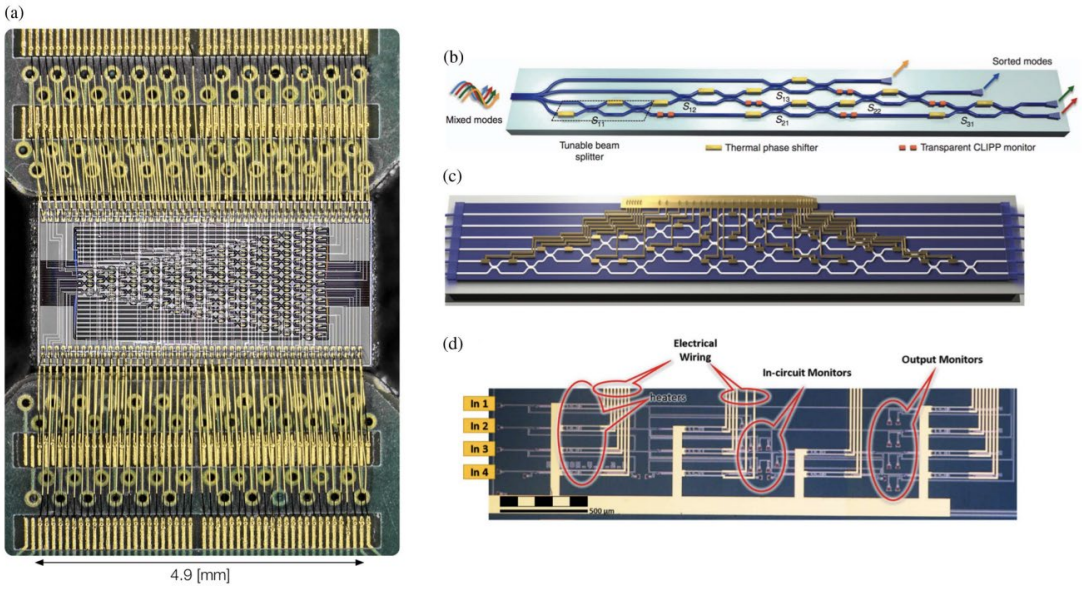

Figure 21: (a) Optical micrograph of 26-mode, 88-MZI PNP. PCBs are visible above and below the chip. (b) Artistic rendering of a U4 PNP by Annoni et al.. (c) Germanium-doped glass six-mode, 15-MZI PNP by Carolan et al.. (d) Four-mode, six-MZI PNP by Ribeiro et al. implemented in the SOI platform.

Configuring or programming N × N mode transformations in a PNP involves precise tuning of approximately N2 phases. This can be a nontrivial problem, especially when considering MZI inhomogeneity and the potential for cross talk between modulators (especially relevant for thermal

modulators). MZI phases are set by applying voltages or currents to each phase shifter, labeled here as (i, j) within the array. Figure 22(c) outlines the basic programming flow. Before considering possible routes towards programming an entire PNP, it is instructive to consider the behavior of a single, programmable MZI. Here, we assumed the differential phase between the two input modes to an MZI can be controlled and is described by some phase γ. Without an external phase shifter (ϕ), transformations are confined to the plane shown in Fig. 22(b). To access the full Poincaré sphere, an external phase shifter is required. A number of programming protocols have been developed, and they can broadly be grouped into one of three categories: (1) element-by-element, with phase shifter settings for each MZI considered individually; (2) compiled, with phase shifter settings for each MZI resulting from a matrix decomposition algorithm[12,13,15]; or (3) optimized, with phase shifter settings for each MZI resulting from the execution of an optimization protocol acting on the phase shifters[15].

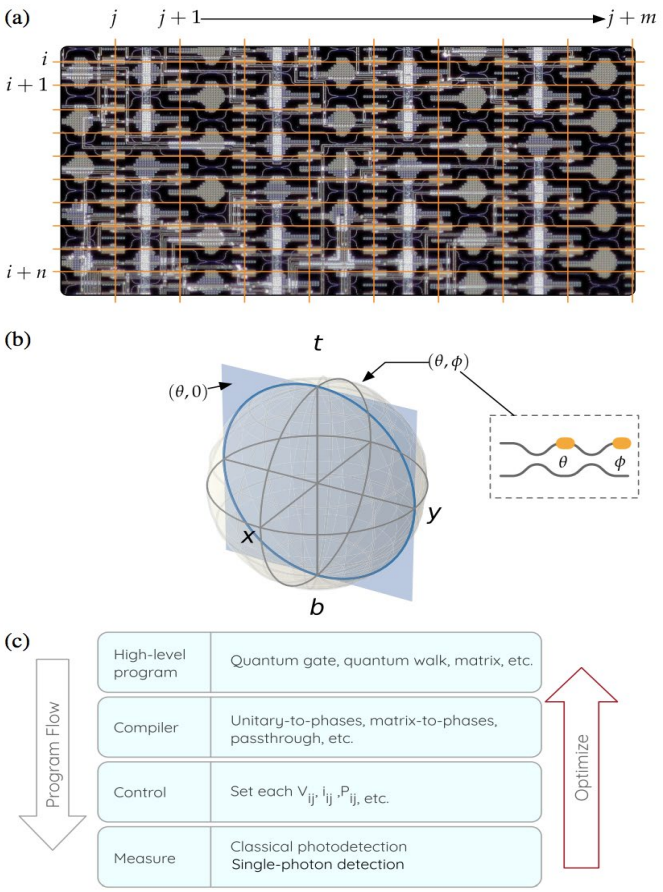

Figure 22: (a) Phase shifter addressing scheme. (b) Poincaré sphere showing the space of transformations enabled between the top "t" and bottom "b" waveguide modes. Without an external phase shifter, transformations are confined to the blue plane; with an external phase shifter, transformations span the sphere. (c) Programming model for programmable nanophotonic processors. After each round of programming, the results of the measurement step can be used to correct the program.

We now discuss a subset of recent PNP applications: self-configuration and mode mixing, quantum transport and quantum gates, and machine learning.

As mentioned above, accurate configuration of the many degrees of freedom (phase settings) in the PNP can pose a challenge, especially when accounting for inhomogeneity in constituent devices. In 2013, Miller proposed a self-configuring solution for one particular PNP function: the coherent addition of light from N spatial input modes into one spatial output mode by canceling the fields in the remaining N − 1 output modes [15]. This concept is illustrated in Figs. 23(a) and 23(b), where the phase shifters of MZIs A–D are consecutively tuned to cancel the photocurrents on the corresponding output detectors. An important advantage in this approach is that each MZI can function without global knowledge of the other MZIs or photodetectors, and this independent self-configuration promises that such coherent, nearly lossless mode adders could be very fast. The coherent field adder only works if the optical modes are locally phase stable; for example, it would be impossible to add single-photon excitations (which have no fixed relative phase) over the input modes. Instead, arbitrary linear optical mode converters require an N × N mesh. Using an extension of his previous work, Miller proposed such a self-configuring N × N mesh that uses detectors on each MZI[32]. Using SOI PIC platforms, a 4 × 4 universal PNP with power monitoring taps was demonstrated in 2016 [27] [see Fig. 20(d)]. A 4 × 4 dynamically self-configuring mode adder was demonstrated in 2017[32]. As shown in Fig. 23(c), the authors used a 980 nm laser to generate a dynamic input state to the 4 × 4 mesh and used CLIPP detectors to actively track and undo mode mixing. As they scale in numbers of modes, self-configuring circuits could enable a range of applications, from spatial multiplexing/demultiplexing—for example in multimode fiber communications—to beam tracking and quantum circuits. The "Clements" architecture cannot be self-configured in this way, though a scheme has been proposed to allow progressive configuration of such networks [14].

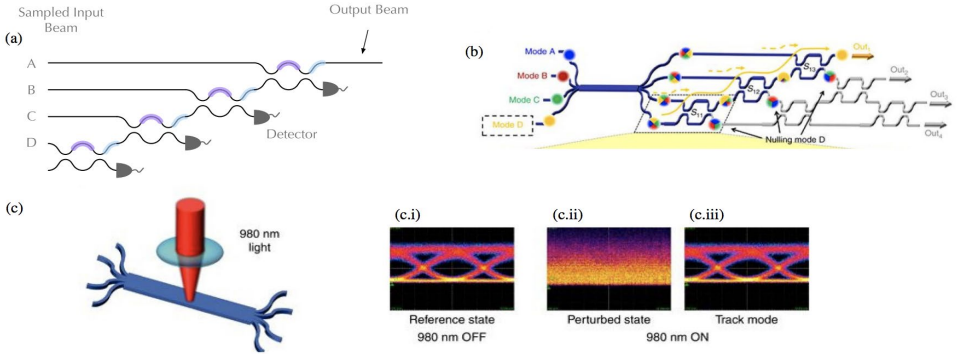

Figure 23: (a) Schematic of system for coherent summing of light from N input spatial modes. (b) Schematic drawing of a U4, Reck-topology PNP with a four-input, four-output multimode interferometer tied to the input waveguides. Active MZIs in this experiment are highlighted blue. (c) To implement dynamic mode mixing, 980 nm light is focused on the multimode interferometer. Eye diagram for signal passing through the mixer (c.i) without the perturbing laser, (c.ii) with the perturbing laser and automatic calibration disabled, and (c.iii) with the perturbing laser and automatic calibration enabled.

A number of interesting problems, from coherent effects in biological processes[33] to quantum computing[34,35] and quantum search, involve the transport of quantum particles along chains of coupled quantum systems. One experimental approach relies on a photonic quantum walk along discrete lattice sites, which can be represented as the waveguides of the PNP. While nonlinear interactions between photons give rise to particularly rich phenomena and applications, even linear quantum walks of single or multiple photons have a number of applications[36–38] and have been proposed to be computationally hard on classical computers for large-enough problems.

Figure 24(a) shows the topology of a 26-mode, fan-out PNP implemented in the silicon photonic platform; this PNP consists of 88 programmable MZIs and 176 phase shifters and supports embeddings of universal unitary circuits up to U9. An input state of photons enters from the left and undergoes a quantum walk on a 1D chain as it passes in time along the right. By programming the splitting ratios of the sites (via the internal phase shift), it is possible to explore discrete-site quantum transport on a number of graphs. In a recent experiment, Harris et al. explored a single photonic quantum walker under static and dynamic phase disorder. Each of the MZIs were set to implement 50:50 splitting ratios, but the external phase shifters were programmed to have either a static phase variation [illustrated in Fig. 24(c)], a dynamically changing phase [illustrated in Fig. 24(d)], or any combination of static and dynamic phase variations. In this configuration, the PNP implements a balanced coin quantum walk on a discrete-time, 1D graph. A sufficiently large static-only phase variation can confine photons to a local vicinity (as in Anderson localization), whereas a strong dynamic phase variation causes a ballistic diffusion in time (due to dephasing between the sites). An optimal trade-off between static and dynamic disorder (which rises with effective system temperature) had been predicted to facilitate environment-assisted exciton transport in photosynthetic complexes[33]. In this regime, dynamic disorder prevents a particle from becoming "stuck" in one site. The programmability of the PNP made it possible to carefully study this quantum transport across 64,400 unique settings of static and dynamic disorder, and demonstrate this environment-assisted quantum transport experimentally.

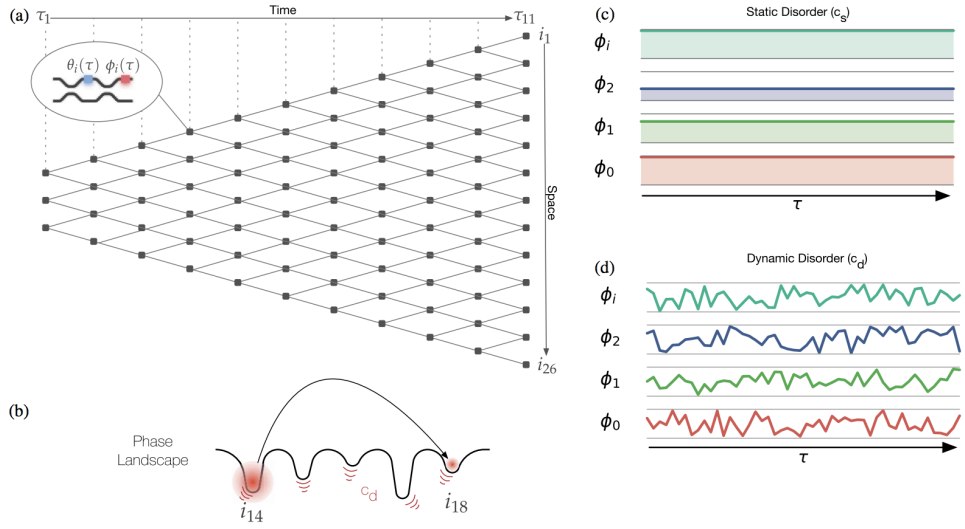

Figure 24: (a) Schematic representation of the 26-mode PNP along with the coordinate system definition for quantum transport experiments. (b) Conceptual drawing of the phase landscape for a strong, statically disordered system where light is localized initially to waveguide i_{14}. By introducing dynamic phase disorder (shown as red vibrations), it is possible to optimize transport of light to distant waveguide sites.

Universal quantum computers follow two predominant frameworks: the circuit model [39], where single qubit and multiqubit gates are performed sequentially on qubits, and the cluster state model[40,41], where a large entangled resource state is first created, and then single qubit gates are performed, which encode the computation. In linear optics photonic quantum computing, two-qubit processes are realized probabilistically. It is therefore critical that the successful operation of a gate be "heralded" by ancillary photons. Carolan et al. used a six-mode PNP alongside an off-chip multiphoton source to implement a variety of heralded gates in both the circuit and cluster state model. Figures 25(a) and 25(b) show the symbol and photonic circuit for a heralded controlled-NOT (CNOT) operation, which uses two path-encoded computational photons and two ancillary photons. Given a detection in the ancillary modes, the CNOT logic is guaranteed to have taken place on the computational photons [see Fig. 25(c)]. Technologically, the low coupling loss of 0.4 dB between silica waveguides and input/output fibers was key to enabling multiphoton experiments of up to six photons. While SOI PNPs have so far been limited to coupling losses of 3 dB, losses as low as 0.4 dB have been demonstrated in silicon photonics, pointing the way towards large-scale SOI PNPs suitable for multiphoton quantum information.

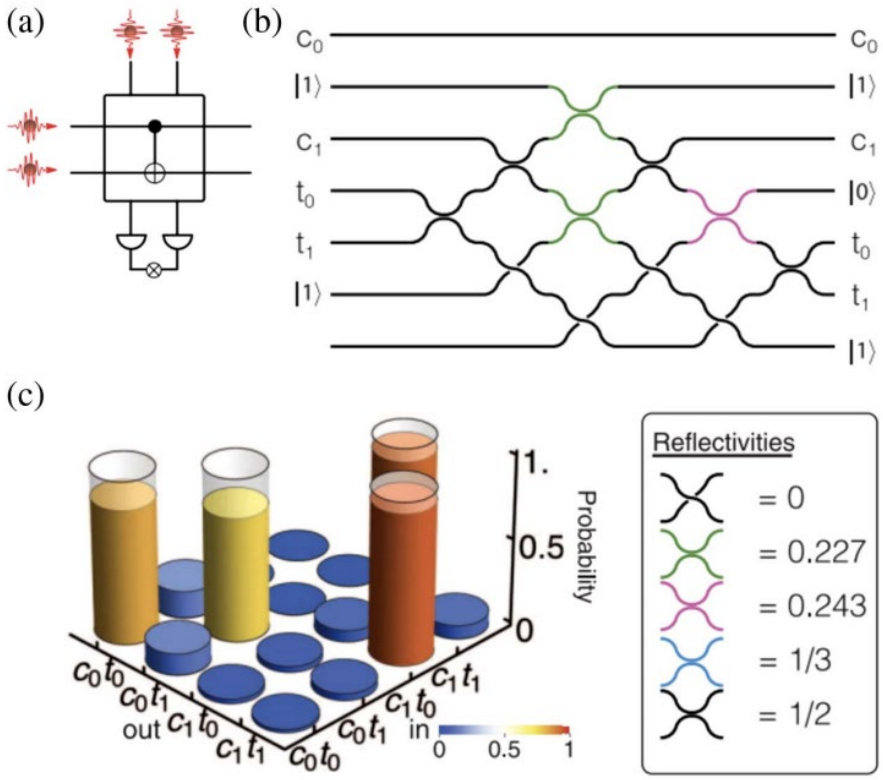

Figure 25: Linear Optical Quantum Logic Gates in a PNP [15]. (a) Heralded controlled-NOT gate schematic. (b) Program within the U6 PNP. (c) Computational truth table, with theoretical result overlaid

4.4 Photon-Photon Interactions in Dynamically Coupled Cavities

The photons are absorbed into the cavity by an effective tuning of its input-output coupling via external control of a coupling to a second, strongly output-coupled cavity mode. Such "dynamically coupled" cavities, which can be implemented using bulk $\chi(2)$ and $\chi(3)$ nonlinearities, enable incoming photon wave packets to be absorbed into the cavity with high fidelity when the duration of the control is similar to that of the wave packets. Further, this configuration can be used to avoid limitations in the photon-photon interaction time set by the delay-bandwidth product of passive cavities and enables the elimination of wave-packet distortions caused by dispersive cavity transmission and reflection. We consider three kinds of nonlinearities, two arising from $\chi(2)$ and $\chi(3)$ materials and one due to an interaction with a two-level emitter. Figure 26 shows the principle of controlled coupling, where an input field is coherently mapped into a second mode. To analyze the input and output of few-photon wave packets, we use a Schrödinger-picture formalism in which traveling-wave fields are discretized into infinitesimal time bins. We suggest that dynamically coupled cavities provide a very useful tool for improving the performance of quantum devices relying on cavity-enhanced light-matter interactions such as single-photon sources and atomlike quantum memories with photon interfaces. As an example, we

present simulation results showing that high-fidelity two-qubit entangling gates may be constructed using any of the considered nonlinear interactions.

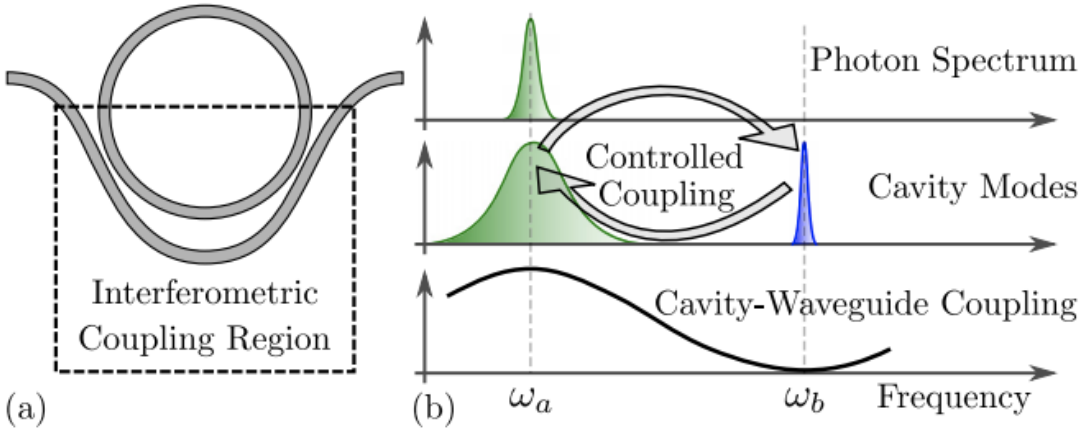

Figure 26: (a) Ring resonator with a Mach-Zehnder interferometer coupling region for frequency-dependent cavity-waveguide coupling rate. (b) Spectra of the incoming photon wave packet (top), cavity modes a (oscillating at ωa) and b (oscillating at ωb) coupled via external control fields (center), and cavity-waveguide coupling rate (bottom).

4.5 Large-scale integration of artificial atoms in hybrid photonic circuits

We greatly exceeded our stated goals on the integration of diamond spin qubits with the AlN-on-sapphire architecture, in the form of diamond waveguides containing individual NV centers. This followed on from our earlier demonstration of such a hybrid integration of diamond qubits with silicon nitride[6], but AlN has far lower autofluorescence. As of Sept 2018, we planned to show that hybrid integration allows devices with at least 8 diamond waveguides containing color center quantum memories on one PIC. By Sept 2019, we had demonstrated 128 functional channels[16], as shown in figure 27, enabled by a hybrid integration pick-and-place approach. Photoluminescence spectroscopy reveals long-term, stable and narrow average optical linewidths of 54 megahertz (146 megahertz) for germanium-vacancy (silicon-vacancy) emitters, close to the lifetime-limited linewidth of 32 megahertz (93 megahertz). We show that inhomogeneities of individual color center optical transitions can be compensated *in situ* by integrated tuning over 50 gigahertz without linewidth degradation. The ability to assemble large numbers of nearly indistinguishable and tunable artificial atoms into phase-stable PICs marks a key step towards multiplexed quantum repeaters and general-purpose quantum processors.

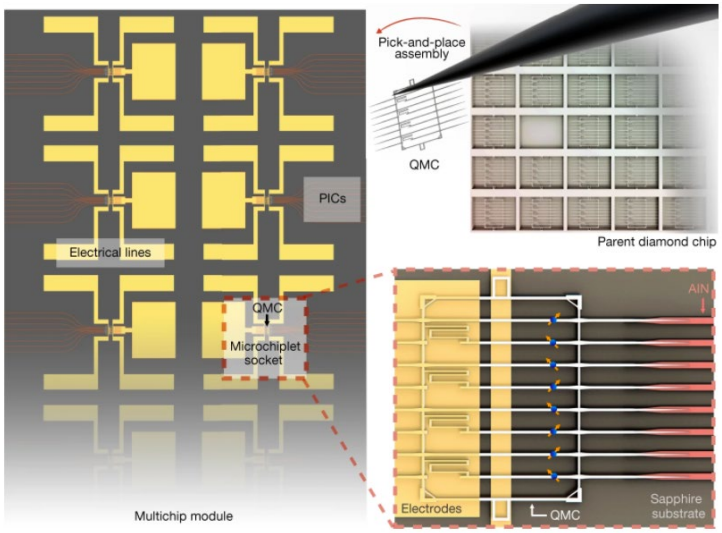

Figure 27: Scalable Integration of Artificial Atoms with Photonics. The separate fabrication of subcomponents before their final assembly maximizes the yield, size and performance of the hybrid emitter–photonics chip. A pick-and-place method transfers pre-screened QMCs from their parent diamond chip into a socket containing efficient photonic interfaces, as well as electrical wires for controlling colour centres.

The large optical transparency of the QMC and PIC materials make them compatible with a variety of quantum emitters. Here we considered the negatively charged germanium-vacancy (GeV) and silicon-vacancy (SiV) centres in diamond with zero-phonon line transitions at 602 nm and 737 nm, respectively, because of their stable optical and spin properties[42,43]. The process begins with focused ion beam (FIB) implantation of Ge^{+} and Si^{+} into a 1-μm-pitch square array in a single-crystal diamond substrate, followed by high-temperature annealing (Methods). This process generated spots of tightly localized GeV centres (depth of about 74 nm, vertical straggle of about 12 nm and lateral full-width at half-maximum (FWHM) distribution of about 40 nm) and SiV centres (about 113 nm, about 19 nm and about 50 nm, respectively), which we then located and mapped relative to prefabricated alignment markers by photoluminescence microscopy. We fabricated the QMCs over the emitter arrays using a combination of electron-beam lithography (EBL) and quasi-isotropic etching. Figure 28a shows a SEM image of various suspended chiplets containing 8- or 16-channel waveguide arrays connected by diamond 'trusses', as seen in the close-up SEM images in Fig. 28b, c and Fig. 28g, respectively. Structurally, much larger arrays are fabricable and integrable: we successfully transferred QMCs with as many as 64 waveguide components (Methods). Despite a misalignment between the FIB mask and the QMC patterns, the photoluminescence scans showed that 39% of the 8-channel QMCs are 'defect free' (that is, they have one or more stable colour centre per waveguide) as shown in Fig. 28e (Methods). The defect-free yield of the 16-channel QMCs was lower as these are more susceptible to misalignment, so we did not use them in this study. With improvements in FIB alignment and lithography, as well as targeted fabrication over pre-localized single emitters, an even higher yield should be possible in future work (Methods).

Figure 28f shows one of 20 micro-chiplet sockets connecting 8 input and 8 output waveguide arrays to an 8-channel QMC. We fabricated this PIC on a wafer of single-crystal AlN on a sapphire substrate using EBL and chlorine reactive ion etching (Methods). AlN on sapphire is a suitable platform for linear and nonlinear quantum photonics because of its large bandgap (about 6.2 eV), high material nonlinearities[44,45] and low narrowband background fluorescence in the spectrum (600–760 nm) of GeV and SiV centres. Using piezo-controlled micromanipulators, we transferred QMCs into the microchiplet sockets with a placement success rate of 90%. The diamond waveguides (width 340 nm and height 200 nm) transfer light into the AlN waveguides (width 800 nm and height 200 nm) through inverse tapered sections with a simulated efficiency of 97% (98%) at a wavelength of 602 nm (737 nm) (Methods). The SEM image of an assembled device in Fig. 25g shows a transverse placement error of 38 ± 16 nm. For such typical errors, simulations indicate a drop in coupling efficiency by 10% or 0.46 dB. We find that the transfer of the QMCs is substantially easier than for individual waveguides due to their rigidity and many alignment features. The successful transfer of 16 defect-free chiplets results in a 128-channel photonically integrated quantum emitter chip, as characterized below.

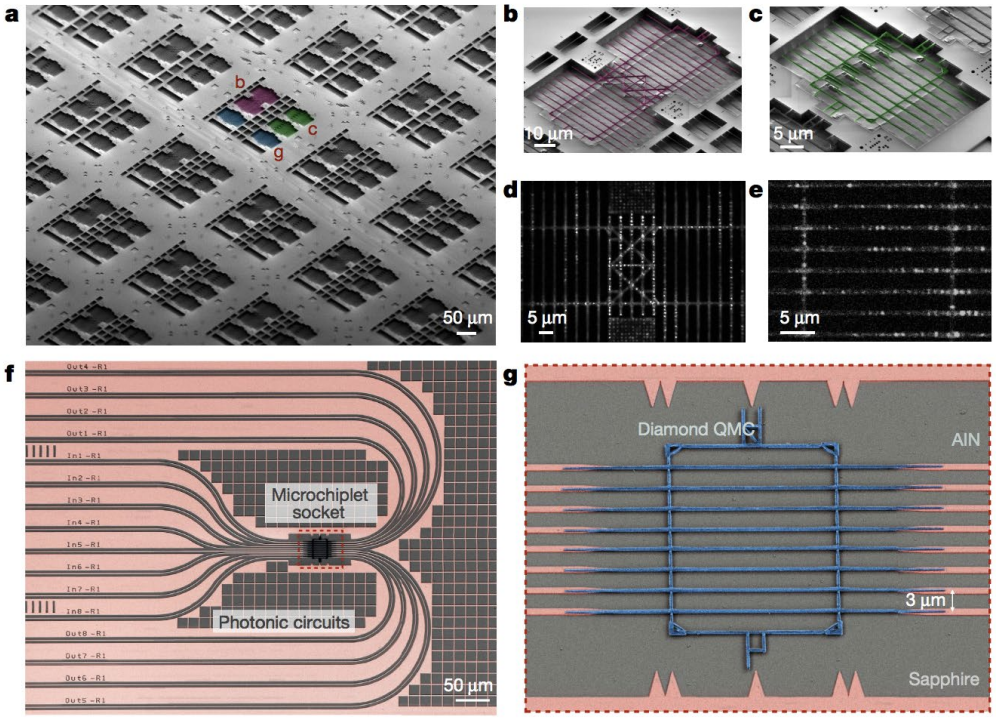

Figure 28: Fabrication and Integration of QMC with Integrated Photonics. a, SEM overview of the parent diamond chip containing over 500 microchiplets for heterogeneous integration. b, A 16-channel QMC. c, An 8-channel QMC with varying mechanical beam rigidity. d, Photoluminescence map of GeV centres (bright spots) in a 16-channel QMC. e, Photoluminescence map of SiV centres (bright spots) in a defect-free 8-channel QMC. f, An AlN-on-sapphire integrated photonics module that interfaces with the diamond QMC placed in the chiplet socket. g, Close-up SEM of the diamond QMC and AlN photonic interfaces.

We performed experiments in a closed-cycle cryostat with a base temperature below 4 K, as illustrated in Fig. 29a. The optical fibre labelled (1) couples pump light (fluorescence) to (from) the QMC via the AlN waveguides. A microscope objective also provides optical access to the QMC, for example, to a colour centre (optical interface labelled (2)) or a scattering site (labelled (3)). Figure 29b shows the energy level and emission spectrum of a single GeV when pumped through (2) and collected through (1). Off-resonant excitation using 532-nm light with off-chip pump filtering in this configuration enables the rapid identification of single emitters (indicated by a photon intensity autocorrelation function $g^{(2)}(0) < 0.5$). The left panel in Fig. 29d shows a typical photon antibunching ($g^{(2)}(0) = 0.19(7)$) from a single GeV centre (channel 41) pumped near saturation, without background or detector jitter correction. Under the resonant excitation at 602 nm of transition C (Fig. 29b) of the zero-phonon line (ZPL), the photon purity improves to $g^{(2)}(0) = 0.06(2)$ (middle panel in Fig. 29d). Similarly, in channel 65, we measured antibunched photons with $g^{(2)}(0) = 0.05(3)$ from a single SiV centre under resonant excitation at 737 nm (right panel in Fig. 29d). In all 128 integrated waveguides, shown in Fig. 29c, we identified single GeV and SiV emitters using top excitation (through (2)) and fibre-coupled waveguide collection (through (1)). Their photon statistics are summarized in Fig. 29e.

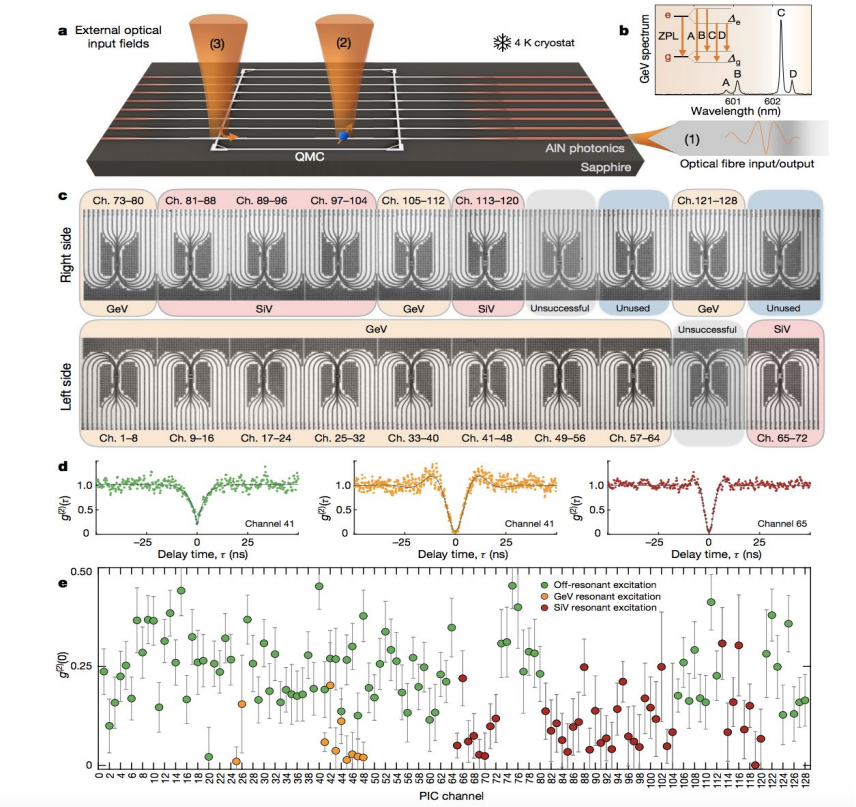

Figure 29: Integrated Quantum Photonics with Colour Centres. a, Experimental setup in a 4-K cryostat showing the input and output optical interfaces (1), (2) and (3). b, Energy level and spectrum of a GeV centre, where g, e, Δg and Δe denote the ground state, excited state, ground-state splitting and excited-state splitting, respectively. Resonant excitation probed transition C, which is the brightest and narrowest line. c, Optical image of sixteen QMC-

populated microchiplet sockets containing GeV or SiV centres. The 'unsuccessful' modules indicate failed QMC placements. Ch., channel. d, Autocorrelation measurements of a single GeV in channel 41 under off-resonant 2-mW, 532-nm excitation (left) and under resonant excitation at 602 nm (middle), and autocorrelation measurement of a single SiV in channel 65 under resonant excitation at 737 nm (right). e, Waveguide-coupled single photons from every integrated GeV and SiV channel in the PIC. The error bars indicate fit uncertainties at the 1 s.d. level.

Next we investigated the optical coherence of a GeV centre using all-fibre spectroscopy. Figure 30a shows the photoluminescence excitation (PLE) spectrum of the channel-41 GeV as we scanned a resonant laser across its ZPL (transition C) with both excitation and detection through the fibre interface (1). Despite the presence of another emitter spectrally detuned by 50 GHz in the same waveguide, resonant excitation allows the selective addressing and readout of single emitters. The measured linewidth of $\Gamma = \Gamma_0 + 2\Gamma_d = 37(3)$ MHz (values in parentheses indicates one standard deviation throughout this work), where Γd is the pure dephasing rate of the emitter, is near the lifetime limit $\Gamma_0 = 1/2\pi\tau = 24(2)$ MHz, as obtained from the excited-state lifetime τ (Methods).

The PIC geometry also enables the direct detection of ZPL resonance fluorescence without any spectral, temporal or polarization filtering, even under resonant excitation. Figure 30b shows the resonance fluorescence obtained for top excitation (through (2)) and waveguide collection without filtering in the detection via (1). By polarizing the pump electric field along the waveguide axis to minimize excitation of the transverse electric waveguide mode, this cross-excitation/detection configuration achieves a ZPL intensity 18 dB above the background, comparable to free-space diamond entanglement experiments using cross-polarization and time-gated detection[18].

According to finite-difference time-domain (FDTD) simulations, an ideal emitter in the optimal configuration has a spontaneous emission coupling efficiency of $\beta = 0.8$ into the diamond waveguide. Experimentally, we measured this efficiency by measuring the transmission of a laser field through a single GeV centre (Fig.30c). By injecting a laser field through (3) and monitoring the transmission T via (1), we observed an extinction of $1 - T = 0.38(9)$ when on resonance with the GeV centre. This extinction places a lower bound of the emitter-waveguide cooperativity at $C = 0.27(10)$ and $\beta = 0.21(6)$. By accounting for residual line broadening and for the ZPL emission fraction (about 0.6), the dipole-waveguide coupling efficiency is at least 0.55(18); see Methods for other factors that reduce β.

The excellent coherence of the GeV centre in channel 41 is not unique. Figure 30d reports the linewidths of every channel in a characteristic 8-channel GeV diamond chiplet, all measured through the on-chip routing of fluorescence into an optical fibre. We found a mean ± standard deviation normalized linewidth of $\Gamma/\Gamma_0 = 1.7 \pm 0.7$, with GeV channels 41, 45 and 48 exhibiting lifetime-limited values of 1.0(2), 0.9(1) and 1.0(2), respectively. From these measurements, we also obtained the inhomogeneous ZPL transition frequency distribution of 85 GHz. In these PLE measurements, we averaged each spectrum over about 5 min (5,000 experiments), demonstrating the emitters' long-term stability after heterogeneous integration. Similarly, as shown in Fig. 30e,

we also found uniformly narrow lines from SiV centres across a QMC, with linewidths within a factor of Γ/Γ0 = 1.6 ± 0.2 from SiV centres in bulk diamond32, and with an inhomogeneous frequency distribution of 30 GHz.

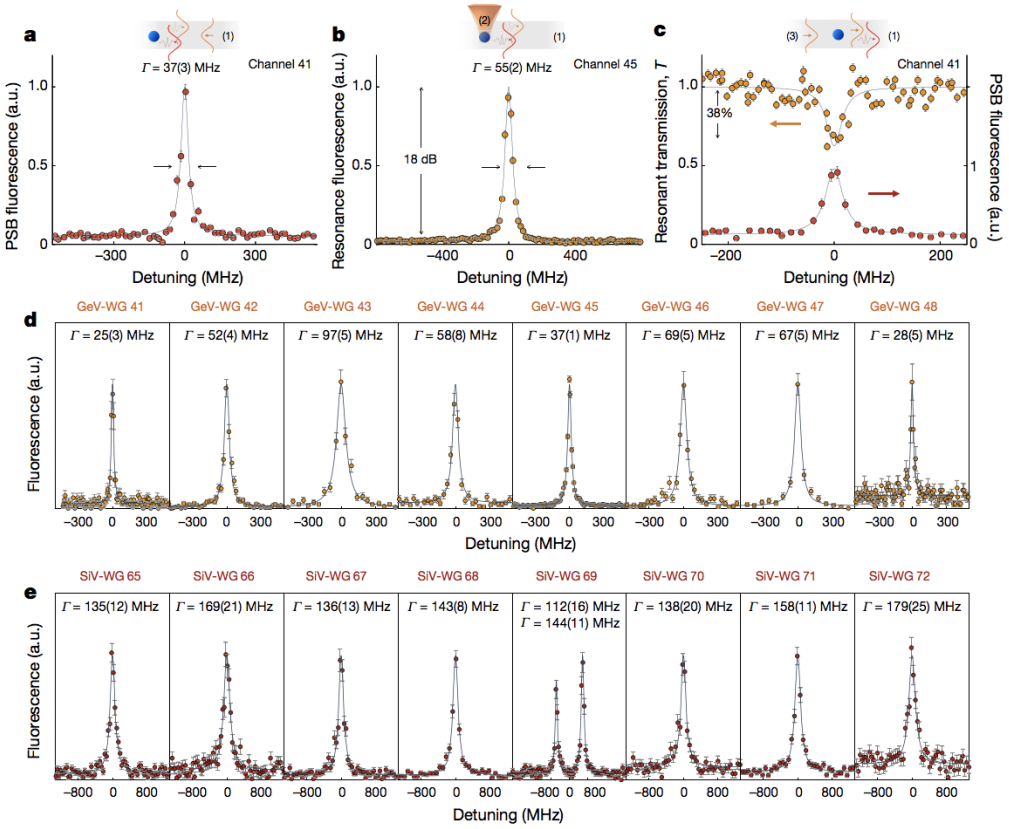

Figure 30: Defect-free Arrays of Optically Coherent and Efficient Waveguide-coupled Emitters. a, PLE spectrum (FWHM linewidth Γ = 37(3) MHz, indicated by the arrows) of a single GeV in channel 41 with all-fibre excitation and detection of the phonon sideband (PSB) fluorescence routed on-chip via (1). b, Excitation via (2) and fluorescence detection via (1). This geometry allows GeV resonance fluorescence detection at least 18 dB above background, without spectral, temporal or polarization filtering. c, In transmission, a single GeV centre causes coherent extinction of ΔT/T = 38(9)% (orange curve, Γ = 35(15) MHz). The red curve shows the PLE spectrum (Γ = 40(5) MHz). d, PLE spectra of GeV centres in each waveguide (WG) of a characteristic 8-channel GeV QMC, with a mean ± standard deviation linewidth of Γ = 54 ± 24 MHz. e, PLE spectra of SiVs in an 8-channel SiV QMC, with Γ = 146 ± 20 MHz. We interpret the two lines in channel 69 as PLE spectra from two distinct SiV centres (g(2)(0) = 0.69(7) under off-resonant excitation, not shown).

To overcome the inhomogeneous spread in transition frequencies, we implemented a strain-tuning scheme using the electrical layers in our PIC. The fabricated device (Fig. 31a, b) uses a QMC that consists of waveguides with different lengths and beam rigidities (Fig. 9). Strain is applied by a capacitive actuator consisting of one gold electrode (Au 1) on the QMC layer, separated transversely by 1.5 μm from a gold ground plane (Au 2) on the sapphire substrate. A bias voltage deforms the waveguide so the associated strain modifies the orbital structures and the optical

transitions of embedded colour centres[18]. This device geometry enables tuning ranges up to 100 GHz, which is larger than the inhomogeneous distribution and only limited by stiction between the QMC and the substrate (Methods). Owing to differences in dipole positions and orientations, we can spectrally overlap the optical transitions of, for example, emitters 1A and 1B in one waveguide at a bias of 24.5 V, as shown in Fig. 31c. Alternatively, they can also be selectively aligned with that of emitter 2, initially detuned by about 10 GHz in another waveguide channel, at distinct voltages. During strain tuning, we did not observe degradation in the linewidths in PLE scans lasting 3 min (Extended Data Fig. 8); this long-term stability remained within 150 MHz over 3 h of continuous measurement without feedback and unchanged up to a tuning of about 6.8 GHz.

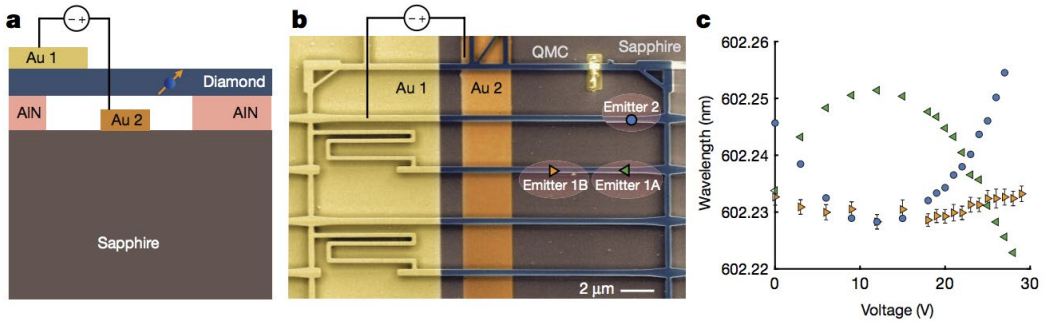

Figure 31: 31 Controlling the Optical Transitions of Colour Centres on a PIC. a, We applied a DC bias between the metal layer Au1 on diamond and metal Au2 on the substrate to electrostatically actuate the QMC. b, SEM image of the device. In this experiment, we investigated the optical response of emitters 1A, 1B and 2 to strain. c, Intra-waveguide emitter 1A and emitter 1B overlap spectrally at 24.5 V. Inter-waveguide overlapping between emitter 2 and emitter 1A (1B) occurs at 2 V (12 V)

4.6 Bright High-Purity Quantum Emitters in Aluminium Nitride Integrated Photonics

Another goal of this program was to investigate color centers in the AlN waveguide material itself. Here, we reported on the optical properties of QEs emitting in the orange visible spectrum integrated in a scalable AlN-on-sapphire PIC platform, as shown in Figure 32. For individual waveguide-integrated QEs, we measured an off-chip count rate exceeding 6×10^4 counts per second (cps) (saturation rate > 8.6×10^4 cps). In an unpatterned thin-film sample, we measure antibunching with $g^{(2)}(0) \sim 0.05$ and photon count rates exceeding 8×10^5 cps (saturation rate > 1×10^6 cps). Although spin and detailed optical linewidth measurements are left for future work, these results already show the potential for high-quality QEs monolithically integrated in a wide range of III-nitride device technologies that would enable new quantum device opportunities and industrial scalability.

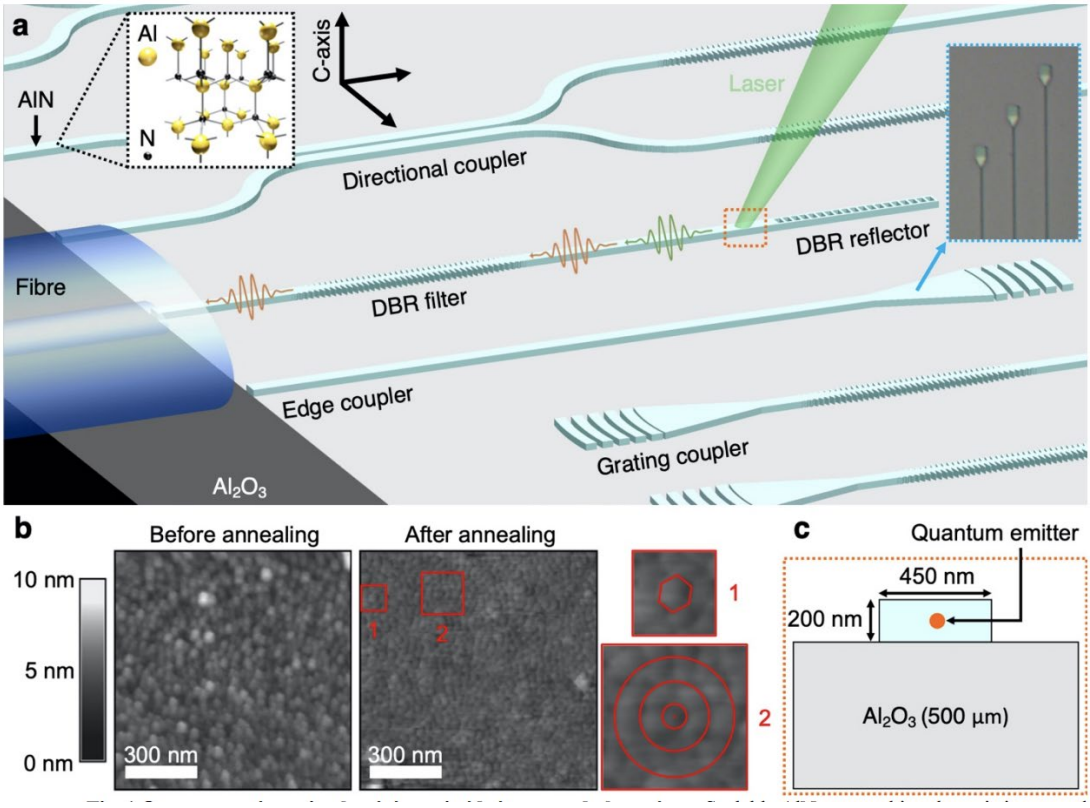

Figure 32: Quantum Emitters in Aluminium Nitride Integrated Photonics. (a) Scalable AlN-on-sapphire photonic integrated circuits with integrated quantum emitters. Black inset: Wurtzite crystal structure of aluminium nitride (yellow: aluminium atom, black: nitrogen atom). Blue inset: Microscope image of the fabricated QE-integrated waveguides, where the grating couplers are used for visual feedback during fibre edge coupling. (b) Atomic force microscopy of a sample before and after annealing. Cutout 1 indicates the hexagonal structure of the nano-columns is maintained after annealing. Cutout 2 shows slight coalescing of the AlN film columnar structure and improved orientation alignment to the c-axis, indicating an improved crystallinity to the AlN film. (c) Close-up cross-section of the single-mode AlN-on-sapphire waveguide, which is 450 nm in width by 200 nm in height. The quantum emitter is embedded within the AlN waveguide (not necessarily in the exact centre as shown).

5.0 CONCLUSION

We have developed, in collaboration with researchers at AFRL Rome Laboratory, Rochester Institute of Technology, BBN Raytheon, and others, a new generation of PIC platforms using a wide-bandgap AlGaN material systems. This work contributes to a promising platform for low-loss integrated photonics across the UV and visible spectrum, including the ability for high power handling, nonlinear optics, electro-optic modulation, and integration with other electro-optic AlGaN components such as optical amplifiers, lasers, and photodetectors. In particular, we showed the integration of the platform with 128 diamond waveguides, each containing one or more high-coherence artificial atoms. In addition, the platform opens up new possibilities in integrated quantum optics with trapped ions or its use for optical control of cold neutral atoms.

$Al_xGa_{1-x}N$-on-AlN is a promising platform for PICs for wavelengths 250nm-to-700nm in the UV-visible range. An Al content x~0.65 results in ~1% lattice mismatch at $Al_xGa_{1-x}N$/AlN interface and a refractive index difference of ~0.1 between these two layers. The latter results in a large single-mode waveguide cross section of multiple wavelengths, relaxing lithographic tolerances and likely lowering scattering losses. In particular, we presented single-mode waveguide designs for TE_0 and TM_0 modes for 300 - 700 nm wavelengths. We also showed that the platform enables compact and high Q resonators, and correspondingly low loss bent waveguides. With a ~1% lattice mismatch between AlGaN and AlN we expected smaller dislocation densities, though the relationship between interface dislocations and optical losses is not presently clear and will need to be explored experimentally. The presented single-crystal UV-vis photonics platform would enable a range of applications including sensing to quantum information science and optical communications.

The UV propagation loss shown here at 369.5 nm was several tens of orders of magnitude lower than the propagation loss shown by Stegmaier et al. for 400 nm wavelength in an AlN on SiO2 platform[28]. Furthermore, the crystalline materials in our AlN on sapphire platform allow for refined Raman and other parasitic processes to be localized and minimized[46]. Although the UV single mode propagation loss presented here is higher than that shown in SiN-on-SiO_2 multimode and planar waveguides for wavelength at the lower end of the visible spectrum[47] and silica-on-silicon waveguides in theory for UV and VIS[48,49], SiN-on-SiO2 and silica-on-silicon platforms are limited to passive components and thermo-optic tuners[50]. Furthermore, silica waveguides are typically a couple of microns in dimension with large bend radii and are not ideal for compact, high-density, large-scale photonic integration. Hence, our AlN on sapphire platform, to date, has the record-low waveguide propagation loss down to UV wavelength for active optical materials with χ (2) properties and supports chip-scale, compact, CMOS-compatible integration[28]. Nonetheless, we believed that there are many sources of loss that can be eliminated or improved upon. One of the main causes for the propagation loss is interface scattering from the roughness of the AlN waveguide sidewalls from etching. To reduce the propagation loss by a few orders of magnitude, one can engineer the waveguide dimensions such that the optical mode overlaps minimally with the sidewalls so that the light scatters minimally from the waveguide's faces[51]. Furthermore, the current waveguide fabrication is optimized for vertical sidewalls so that the photonic components experimentally match well with the simulated design. As such, the reactive-ion etching necessitates a fast physical etch that causes the sidewalls to be rougher than could be possible with

a more chemical etch. Sidewall roughness of less than 0.1 nm is often the benchmark for achieving interface scattering close to that of the bulk scattering limit of optical materials. It may be possible to further optimize the etching parameters to reduce loss. In addition, there is an inherent roughness of the top surface of the AlN thin film from the unoptimized growth. As AlN grown on top of sapphire is still not at the level of silicon on insulator (SOI) wafers made by Smart-Cut technology used in conventional integrated photonic platforms, we expected there to be room for improvements. Finally, the AlN thin film we used is crystalline in the growth direction and polycrystalline in the in-plane direction. Replacing this material with a completely crystalline AlN thin film grown on top of sapphire should result in a lower dislocation density and defect density, thereby improving the purity of our material so that it would behave closer to what is expected of bulk AlN. Furthermore, the crystallinity of single-crystal AlN grown on top of sapphire has been shown to improve significantly by high temperature annealing[52]. The nonlinear susceptibilities χ (2) and χ (3) of AlN are material dependent and approximately independent of the film crystallinity, even when taking into account small variation due to crystal stress/strain during growth. However, the effective nonlinearity experienced for nanocrystalline AlN will have a reduced percentage of that intended crystal axis in the field propagation direction of the waveguide mode, thus reducing the effective nonlinearity when compared to epitaxially grown single crystal AlN. As such, further improvements on the crystallinity of AlN thin film grown on top of sapphire would be beneficial for nonlinear applications as well.

6.0 REFERENCES

1. Soltani, M., Soref, R., Palacios, T. & Englund, D. AlGaN/AlN integrated photonics platform for the ultraviolet and visible spectral range. *Opt. Express* **24**, 25415–25423 (2016).
2. Heuck, M., Jacobs, K. & Englund, D. R. Controlled-Phase Gate Using Dynamically Coupled Cavities and Optical Nonlinearities. *Phys. Rev. Lett.* **124**, 160501 (2020).
3. Heuck, M., Jacobs, K. & Englund, D. R. Photon-photon interactions in dynamically coupled cavities. *Phys. Rev. A* (2020).
4. Patra, A., Tallman, R. E. & Weinstein, B. A. Effect of crystal structure and dopant concentration on the luminescence of Cr3+ in Al2O3 nanocrystals. *Opt. Mater.* **27**, 1396–1401 (2005).
5. Parkhomenko, I. *et al.* Origin of visible photoluminescence from Si-rich and N-rich silicon nitride films. *Thin Solid Films* **626**, 70–75 (2017).
6. Mouradian, S. L. *et al.* Scalable Integration of Long-Lived Quantum Memories into a Photonic Circuit. *Phys. Rev. X* **5**, 031009 (2015).
7. Monroe, C. & Kim, J. Scaling the ion trap quantum processor. *Science* **339**, 1164–1169 (2013).
8. Goban, A. *et al.* Atom-light interactions in photonic crystals. *Nat. Commun.* **5**, 3808 (2014).
9. Miller, D. A. B. Perfect optics with imperfect components. *Optica, OPTICA* **2**, 747–750 (2015).
10. Carolan, J. *et al.* QUANTUM OPTICS. Universal linear optics. *Science* **349**, 711–716 (2015).
11. Absil, P. P. *et al.* Imec iSiPP25G silicon photonics: a robust CMOS-based photonics

technology platform. in vol. 9367 93670V (International Society for Optics and Photonics, 2015).

12. Reck, M., Zeilinger, A., Bernstein, H. J. & Bertani, P. Experimental realization of any discrete unitary operator. *Phys. Rev. Lett.* **73**, 58–61 (1994).
13. Clements, W. R., Humphreys, P. C., Metcalf, B. J., Steven Kolthammer, W. & Walmsley, I. A. Optimal design for universal multiport interferometers. *Optica, OPTICA* **3**, 1460–1465 (2016).
14. Miller, D. A. B. Self-aligning universal beam coupler. *Opt. Express* **21**, 6360–6370 (2013).
15. Miller, D. A. B. Self-configuring universal linear optical component [Invited]. *Photon. Res., PRJ* **1**, 1–15 (2013).
16. Wan, N. H. *et al.* Large-scale integration of artificial atoms in hybrid photonic circuits. *Nature* **583**, 226–231 (2020).
17. Maity, S. *et al.* Spectral Alignment of Single-Photon Emitters in Diamond using Strain Gradient. *Phys. Rev. Applied* **10**, 024050 (2018).
18. Meesala, S. *et al.* Strain engineering of the silicon-vacancy center in diamond. *Phys. Rev. B Condens. Matter* **97**, 205444 (2018).
19. Sohn, Y.-I. *et al.* Controlling the coherence of a diamond spin qubit through its strain environment. *Nat. Commun.* **9**, 2012 (2018).
20. Maier, F., Riedel, M., Mantel, B., Ristein, J. & Ley, L. Origin of surface conductivity in diamond. *Phys. Rev. Lett.* **85**, 3472–3475 (2000).
21. Soltani, M. & Soref, R. Free-carrier electrorefraction and electroabsorption in wurtzite GaN. *Opt. Express* **23**, 24984–24990 (2015).
22. Kao, C.-K. *et al.* A comparative study of UV electro-absorption modulators based on bulk

III-nitride films and multiple quantum wells. *Phys. Status Solidi C* **9**, 770–773 (2012).

23. Bickermann, M. *et al.* UV transparent single-crystalline bulk AlN substrates. *Phys. Status Solidi C* **7**, 21–24 (2010).
24. Dalmau, R. *et al.* Growth and Characterization of AlN and AlGaN Epitaxial Films on AlN Single Crystal Substrates. *J. Electrochem. Soc.* **158**, H530 (2011).
25. Zhu, D., Wallis, D. J. & Humphreys, C. J. Prospects of III-nitride optoelectronics grown on Si. *Rep. Prog. Phys.* **76**, 106501 (2013).
26. Jianchang, Y. *et al.* High quality AlGaN grown on a high temperature AIN template by MOCVD. *J. Semicond.* **30**, 103001 (2009).
27. Hirayama, H., Maeda, N., Fujikawa, S., Toyoda, S. & Kamata, N. Recent progress and future prospects of AlGaN-based high-efficiency deep-ultraviolet light-emitting diodes. *Jpn. J. Appl. Phys.* **53**, 100209 (2014).
28. Lu, T.-J. *et al.* Aluminum nitride integrated photonics platform for the ultraviolet to visible spectrum. *Opt. Express* **26**, 11147–11160 (2018).
29. Zhu, D. *et al.* A scalable multi-photon coincidence detector based on superconducting nanowires. *arXiv [physics.ins-det]* (2017).
30. Harris, N. C., Carolan, J., Bunandar, D. & Prabhu, M. Linear programmable nanophotonic processors. *Optica* (2018).
31. Watts, M. R. Adiabatic microring resonators. *Opt. Lett.* **35**, 3231–3233 (2010).
32. Annoni, A. *et al.* Unscrambling light-automatically undoing strong mixing between modes. *Light Sci Appl* **6**, e17110 (2017).
33. Rebentrost, P., Mohseni, M., Kassal, I., Lloyd, S. & Aspuru-Guzik, A. Environment-assisted quantum transport. *New J. Phys.* **11**, 033003 (2009).

34. Lahini, Y., Steinbrecher, G. R., Bookatz, A. D. & Englund, D. Quantum logic using correlated one-dimensional quantum walks. *npj Quantum Information* **4**, 2 (2018).

35. Childs, A. M., Gosset, D. & Webb, Z. Universal computation by multiparticle quantum walk. *Science* **339**, 791–794 (2013).

36. Crespi, A. *et al.* Anderson localization of entangled photons in an integrated quantum walk. *Nat. Photonics* **7**, 322–328 (2013).

37. Peruzzo, A. *et al.* Quantum walks of correlated photons. *Science* **329**, 1500–1503 (2010).

38. Sparrow, C. *et al.* Simulating the vibrational quantum dynamics of molecules using photonics. *Nature* **557**, 660–667 (2018).

39. Nielsen, M. A. & Chuang, I. Quantum Computation and Quantum Information. *Am. J. Phys.* **70**, 558–559 (2002).

40. Raussendorf, R., Browne, D. E. & Briegel, H. J. Measurement-based quantum computation on cluster states. *Phys. Rev. A* **68**, 022312 (2003).

41. Raussendorf, R. & Briegel, H. J. A one-way quantum computer. *Phys. Rev. Lett.* **86**, 5188–5191 (2001).

42. Sukachev, D. D. *et al.* Silicon-Vacancy Spin Qubit in Diamond: A Quantum Memory Exceeding 10 ms with Single-Shot State Readout. *Phys. Rev. Lett.* **119**, 223602 (2017).

43. Bhaskar, M. K. *et al.* Quantum Nonlinear Optics with a Germanium-Vacancy Color Center in a Nanoscale Diamond Waveguide. *Phys. Rev. Lett.* **118**, 223603 (2017).

44. Xiong, C., Pernice, W. H. P. & Tang, H. X. Low-loss, silicon integrated, aluminum nitride photonic circuits and their use for electro-optic signal processing. *Nano Lett.* **12**, 3562–3568 (2012).

45. Jung, H., Xiong, C., Fong, K. Y., Zhang, X. & Tang, H. X. Optical frequency comb

generation from aluminum nitride microring resonator. *Opt. Lett.* **38**, 2810–2813 (2013).

46. Liu, X. *et al.* Aluminum nitride-on-sapphire platform for integrated high-Q microresonators. *Opt. Express* **25**, 587–594 (2017).
47. Gorin, A., Jaouad, A., Grondin, E., Aimez, V. & Charette, P. Fabrication of silicon nitride waveguides for visible-light using PECVD: a study of the effect of plasma frequency on optical properties. *Opt. Express* **16**, 13509–13516 (2008).
48. Lee, H., Chen, T., Li, J., Painter, O. & Vahala, K. J. Ultra-low-loss optical delay line on a silicon chip. *Nat. Commun.* **3**, 867 (2012).
49. Yoon Oh, D. *et al.* Coherent ultra-violet to near-infrared generation in silica ridge waveguides. *Nat. Commun.* **8**, 13922 (2017).
50. Heck, M. J. R., Bauters, J. F., Davenport, M. L., Spencer, D. T. & Bowers, J. E. Ultra-low loss waveguide platform and its integration with silicon photonics. *Laser Photonics Rev.* **8**, 667–686 (2014).
51. Miller, S. A. *et al.* Low-loss silicon platform for broadband mid-infrared photonics. *Optica, OPTICA* **4**, 707–712 (2017).
52. Miyake, H., Lin, C.-H., Tokoro, K. & Hiramatsu, K. Preparation of high-quality AlN on sapphire by high-temperature face-to-face annealing. *J. Cryst. Growth* **456**, 155–159 (2016).

APPENDIX A: Publications and Presentations

Journal Publications on RITA FA8750-16-2-0141:

1. Mohammad Soltani, Richard Soref, Tomas Palacios, Dirk Englund, ``AlGaN/AlN integrated photonics platform for the ultraviolet and visible spectral range," Optics Express 24 (22), pp. 25415-25423 (2016)

2. Tsung-Ju Lu, Michael Fanto, Hyeongrak Choi, Paul Thomas, Jeffrey Steidle, Sara L. Mouradian, Wei Kong, Di Zhu, Hyowon Moon, Karl Berggren, Jeehwan Kim, Mohammad Soltani, Stefan Preble, Dirk Englund, ``An Aluminum Nitride Integrated Photonics Platform for the Ultraviolet to Visible Spectrum," Optics Express 26, 9, pp. 11147-11160 (2018)

3. Nicholas Harris, Jacques Carolan, Darius Bunandar, Michael Hochberg, Thomas Baehr-Jones, Michael Fanto, A Smith, Christopher Tison, Mihika Prabhu, Paul Alsing, Dirk Englund, ``Linear programmable nanophotonic processors," Optica Vol. 5, Issue 12, pp. 1623-1631 (2018)

4. Mikkel Heuck, Kurt Jacobs, Dirk Englund, ``Photon-Photon Interactions in Dynamically Coupled Cavities," Phys. Rev. A 101, 042322 (2020)

5. Noel H. Wan*, Tsung-Ju Lu*, Kevin C. Chen, Michael P. Walsh, Matthew E. Trusheim, Lorenzo De Santis, Eric Bersin, Ian Christen, Isaac B. Harris, Sara L. Mouradian, Edward S. Bielejec, Dirk Englund, ``Large-scale integration of artificial atoms in hybrid photonic circuits," Nature 583, pages 226–23 (2020)

6. Tsung-Ju Lu*, Benjamin Lienhard*, Kwang-Yong Jeong, Hyowon Moon, Ava Iranmanesh, Gabriele Grosso, Dirk Englund, ``Bright High-Purity Quantum Emitters in Aluminium Nitride Integrated Photonics," ArXiv 2006.16276 (2020). Under review.

Patents

- Application Number: US 16/734,727; Title: Scalable Integration of Hybrid Optoelectronic and Quantum Optical Systems into Photonic Circuits. Filing Date: January 06, 2020. Inventor(s): WAN et al.. MIT 21263. Smith Baluch MIT-21263US01

Conferences

1. Dirk Englund, "Photonic Integrated Circuits for Quantum Communications," U. of Stuttgart Physik Kolloqium (2017)
2. Dirk Englund, "Semiconductor Quantum Technologies for Communications and Computing," Niels Bohr Institute Colloquium (2017)
3. Dirk Englund, "Networking Quantum Memories on Photonic Integrated Circuits," Physikalisches Kolloquium, Department für Physik FAU Erlangen-Nürnberg (2017)
4. Dirk Englund, "Semiconductor Quantum Technologies for Communications and Computing," Center for Ultracold Atoms, MIT (2017)
5. Dirk Englund, "Quantum Information Processing with Spins and Photons in Semiconductor Circuits," Vienna Physics Colloquium (2017)
6. Dirk Englund, "Networking Quantum Memories on Photonic Integrated Circuits," Macquarie University, Sydney (2017)
7. Dirk Englund, "Photonic Integrated Circuits for Repeater-Based Range Quantum Communications," University of Technology Sydney (2017)
8. Dirk Englund, "Semiconductor Quantum Technologies for Communications and Computing," University of Michigan ECE Colloquium (2017)
9. Dirk Englund, "Semiconductor Quantum Technologies for High-Speed and Long-Range Quantum Communications," CUDOS Annual Meeting (2017)
10. Benjamin Lienhard, Tsung-Ju Lu, Kwang-Yong Jeong, Hyowon Moon, Ava Iranmanesh, Gabriele Grosso, Dirk Englund, "High-Purity Single-Photon Emitter in Aluminum Nitride," APS March Meeting (2017)
11. Benjamin Lienhard, Tsung-Ju Lu, Kwang-Yong Jeong, Hyowon Moon, Ava Iranmanesh, Gabriele Grosso, Dirk Englund, "High-Purity Single Photon Emitter in Aluminum Nitride Photonic Integrated Circuit," CLEO Europe (2017)
12. Dirk Englund, "Semiconductor Quantum Technologies for High-Speed and Long-Distance Quantum Communications," Northwestern University Physics Symposium (2017)
13. Dirk Englund, "Semiconductor quantum technologies for communications and computing," 24th Central European Workshop on Quantum Optics, Denmark Technical University, Copenhagen (2017)
14. Dirk Englund, " Semiconductor Quantum Technologies for High-Speed Quantum Communications and Modular Quantum Computers," Laboratory for Physical Sciences (2017)
15. Dirk Englund, "Quantum Sensing and Imaging using Color Centers in Diamond: Towards neuronal voltage imaging ," MRS Spring Meeting; Phoenix, Arizona (2017)

16. Dirk Englund, "2D Materials Optoelectronic Devices for Quantum Information Processing and Sensing," Graphene 2017; Barcelona, March 29th (2017)

17. Dirk Englund, "Quantum Secure Communications: Status and Outlook," The Impact of Emerging Quantum Information on Information Fusion: Panel Presentation - SPIE DEFENSE - Anaheim, CA (2017)

18. Dirk Englund, "Engineering semiconductor quantum memories for quantum networks ," NSF Frontiers of Condensed Matter Physics, Arlington VA (2017)

19. Dirk Englund, "Semiconductor Quantum Technologies for Secure Communications and Scalable Quantum Networks," Applied Physics Seminar, Caltech, April (2017)

20. Dirk Englund, "Large-scale photonic circuits for quantum information processing and machine learning," SPIE DEFENSE - Anaheim, CA (2017)

21. Dirk Englund, "Towards On-Chip Quantum Networks with Diamond Spins," OSA Incubator on Integrated Semiconductor Quantum Photonic Devices; Washington, DC (2017)

22. Dirk Englund, "Towards Scalable Semiconductor Quantum Technologies," Master Dynamic Opening Ceremony “Ignite Technology in Hong Kong” (2017)

23. Nicholas Harris; Yichen Shen; Gregory Steinbrecher; Mihika Prabhu; Tom Baehr-Jones; Michael Hochberg; Marin Soljacic; Dirk Englund, "Programmable Nanophotonics for Quantum Simulation and Machine Learning," Advanced Photonics 2017 (2017)

24. Dirk Englund, "Semiconductor quantum technologies for communications and computing," CEWQO 2017 - 24th Central European Workshop on Quantum Optics (2017)

25. Dirk Englund, "Towards Scalable Semiconductor Quantum Networks," META Conference - Incheon, Korea (2017)

26. Tsung-Ju Lu, Hyeongrak Choi, Michael Fanto, Paul Thomas, Jeffrey Steidle, Sara L. Mouradian, Wei Kong, Di Zhu, Hyowon Moon, Karl K. Berggren, Jeehwan Kim, Mohammad Soltani, Stefan Preble, and Dirk Englund, "An Aluminum Nitride Integrated Photonics Platform for the Ultraviolet to Visible Spectrum," MRS Fall Meeting 2017 (2017)

27. Tsung-Ju Lu, Michael Fanto, Hyeongrak Choi, Paul Thomas, Jeffrey Steidle, Sara L. Mouradian, Wei Kong, Di Zhu, Hyowon Moon, Karl K. Berggren, Jeehwan Kim, Mohammad Soltani, Stefan Preble, and Dirk Englund, "An Aluminum Nitride Integrated Photonics Platform for the Ultraviolet to Visible Spectrum," CLEO 2018 (2018)

28. D Englund, "Semiconductor Quantum Technologies for Secure Communications and Quantum Networks," QuTec Seminar, Delft University of Technology, Netherlands (2018)

29. Matthew E. Trusheim, Edward Bielejec, Dirk Englund, "Scalable Nanoscale Patterning of Quantum Emitters in Diamond via Focused Ion Beam," CAARI 2018 (2018)

30. Ryan Hamerly, "Quantum vs. Optical Annealing: the Coherent Ising Machine and D-Wave," UMass-Lowell Theoretical Physics Seminar (10/26/2018)

31. Ryan Hamerly, "Quantum vs. Optical Annealing: the Coherent Ising Machine and D-Wave," Seminar at Todai (host: Prof. Takuo Tanemura) (11/5/2018)

32. Ryan Hamerly, "Large-Scale Energy-Efficient Optical Neural Networks based on Coherent Detection," Seminar at TU-Dresden (host: Prof. Kambiz Jamshidi) (11/20/2018)

33. Ryan Hamerly, "Large-Scale Energy-Efficient Optical Neural Networks based on Coherent Detection," Seminar at TU-Eindhoven (Koonen group) (11/26/2018)

34. D Englund, "Towards Arrays of Designer Artificial Atoms for Scalable Quantum Technologies," Atom by Atom Fabrication Workshop; Oak Ridge National Laboratory | Nov 2, 2018 (2018)

35. Dirk Englund, "Large-Scale Photonic Circuits for Quantum Information Processing," Photonics for Quantum Conference, Rochester Institute of Technology | Rochester, NY (1/25/2019)

36. Dirk Englund, "Large-Scale Photonic Circuits for Quantum Information Processing," PQE 2019, Utah (1/8/2019)

37. Dirk Englund, "From modular quantum computers .. to all-optical architectures," Defense Science Board, Draper Laboratories | Cambridge, MA (12/11/2018)

38. Dirk Englund, "Silicon Photonics for Quantum Information Processing and Machine Learning," OFC | March 4, 2019 | San Diego, California (3/4/2019)

39. Liane Bernstein, Alexander Sludds, Ryan Hamerly, Dirk Englund, "Scalable Free-Space Optical Neural Networks," APS March Meeting (3/6/2019)

40. Dirk Englund, "Large-Scale Photonic Integrated Circuits for Multiplexed Quantum Repeaters," Q.Link.X-Status Meeting, Bonn, Germany (6/7/2019)

41. Dirk Englund, "Photonics for Scaling: Quantum and Classical Information Processing ," Army Research Office, Durham, NC 27703 (6/3/2019)

42. Dirk Englund, "CLEO Short Course SC455: Integrated Photonics for Quantum Information Science and Technology," CLEO: QELS_Fundamental Science, Optical Society of America, 2013** (5/7/2019)

43. Dirk Englund, "Scalable Quantum Networks with Artificial Atoms ," Physics Colloquium: The City College of New York, NY (5/15/2019)

44. Dirk Englund, "Photonic Integrated Circuits with Multiplexed Quantum Memories for Quantum Networks," LATSIS Conference, EPFL - Lausanne, Switerland (5/20/2019)

45. Dirk Englund, "Scalable Quantum Networks with Artificial Atoms ," Joint Quantum Symposium, Columbia University, New York City (4/19/2019)

46. Dirk Englund, "Quantum Memory-Integrated Photonic Circuits for Quantum Networks," Optical Fiber Conference (OFC), San Diego, California (3/6/2019)

47. Dirk Englund, "Scalable Quantum Networks with Artificial Atoms ," SCALABLE INFORMATION PROCESSING WITH QUANTUM NANO-PHOTONICS (SIPQNP) CONFERENCE, Tucson, AZ (3/26/2019)

48. Dirk Englund, "Optical Accelerators for Machine Learning," NTT Physics of Information - Seminar; Palo Alto, CA (7/9/2019)

49. Liane Bernstein, Alexander Sludds, Ryan Hamerly, Dirk Englund, "Neuromorphic Photonics," Fast Machine Learning (IRIS-HEP Blueprint) (9/11/2019)

50. Ryan Hamerly, "Quantum vs. Optical Annealing: Benchmarking the Coherent Ising Machine and D-Wave 2000Q on NP-hard Ising Problems," PQE 2019 (1/7/2019)

51. Ryan Hamerly, "Benchmarking coherent Ising machines and quantum annealers with MAX-CUT and SK problems," APS March Meeting (3/6/2019)

52. Ryan Hamerly, "Scaling advantages of all-to-all connectivity for NP-hard Ising problems," Coherent Network Computing 2019 (3/20/2019)

53. Ryan Hamerly, "Large-scale optical neural networks based on quantum photoelectric multiplication," MIT Quest AI workshop (5/7/2019)

54. Ryan Hamerly, "Large-scale optical neural network accelerators based on coherent detection," CLEO 2019 (5/10/2019)

55. Ryan Hamerly, "Large-scale nanophotonic neural networks based on coherent detection," PICS 2019 (6/21/19)

56. Ryan Hamerly, "Connectivity and benchmarking quantum annealers," HPM 2019 (9/30/2019)

57. Ryan Hamerly, "Towards large-scale photonic neural network accelerators," IEDM 2019 (12/10/2019)

58. Ryan Hamerly, "Scalable time multiplexed optical neural networks based on homodyne detection," FiO+LS 2019 (9/18/2019)

59. Noel H. Wan et al, "A 128-channel diamond quantum memory array integrated in a microphotonic chip," CLEO 2020 (5/11/2020)

60. Noel H. Wan et al, "A 72-Channel Diamond Quantum Memory Array Integrated in a Microphotonic Chip," MRS Fall 2019 (12/3/2019)

61. Noel H. Wan et al, "Engineering scalable optical interfaces for diamond spin qubits," GRC Quantum Science 2018 (7/28/2018)

62. Dirk Englund, "Large-Scale Photonic Circuits for Quantum Information Processing," Photonic quantum information processing: DARPA Information Meeting (2/19/2020)

63. Dirk Englund, "Programmable Photonic Circuits for Quantum Information Processing & Machine Learning," CLEO 2020: Session on Integrated Quantum Photonics: Circuits (FF2D)a (5/15/2020)

APPENDIX B: Abstracts

AlGaN/AlN Integrated Photonics Platform for the Ultraviolet and Visible Spectral Range: We analyze a photonic integrated circuit (PIC) platform comprised of a crystalline AlxGa1-xN optical guiding layer on an AlN substrate for the ultraviolet to visible (UV-vis) wavelength range. An Al composition of x~0.65 provides a refractive index difference of ~0.1 between AlxGa1-xN and AlN, and a small lattice mismatch (< 1%) that minimizes crystal dislocations at the AlxGa1-xN/AlN interface. This small refractive index difference is beneficial at shorter wavelengths to avoid extra-small waveguide dimensions. The platform enables compact waveguides and bends with high field confinement in the wavelength range from 700 nm down to 300 nm (and potentially lower) with waveguide cross-section dimensions comparable to those used for telecom PICs such as silicon and silicon nitride waveguides, allowing for well-established optical lithography. This platform can potentially enable cost-effective, manufacturable, monolithic UV-vis photonic integrated circuits.

An Aluminum Nitride Integrated Photonics Platform for the Ultraviolet to Visible Spectrum : We demonstrate a wide-bandgap semiconductor photonics platform based on nanocrystalline aluminum nitride (AlN) on sapphire. This photonics platform guides light at low loss from the ultraviolet (UV) to the visible spectrum. We measure ring resonators with intrinsic quality factor (Q) exceeding 170,000 at 638 nm and Q >20,000 down to 369.5 nm, which shows a promising path for low-loss integrated photonics in UV and visible spectrum. This platform opens up new possibilities in integrated quantum optics with trapped ions or atom-like color centers in solids, as well as classical applications including nonlinear optics and on-chip UV-spectroscopy

Linear Programmable Nanophotonic Processors: Advances in photonic integrated circuits have recently enabled electrically reconfigurable optical systems that can implement universal linear optics transformations on spatial mode sets. This review paper covers progress in such "programmable nanophotonic processors" as well as emerging applications of the technology to problems including classical and quantum information processing and machine learning.

Photon-Photon Interactions in Dynamically Coupled Cavities: We study theoretically the interaction between two photons in a nonlinear cavity. The photons are absorbed into the cavity by an effective tuning of its input-output coupling via external control of a coupling to a second, strongly output-coupled cavity mode. Such "dynamically coupled" cavities, which can be implemented using bulk $\chi(2)$ and $\chi(3)$ nonlinearities, enable incoming photon wave packets to be absorbed into the cavity with high fidelity when the duration of the control is similar to that of the

wave packets. Further, this configuration can be used to avoid limitations in the photon-photon interaction time set by the delay-bandwidth product of passive cavities and enables the elimination of wave-packet distortions caused by dispersive cavity transmission and reflection. We consider three kinds of nonlinearities, two arising from $\chi(2)$ and $\chi(3)$ materials and one due to an interaction with a two-level emitter. To analyze the input and output of few-photon wave packets, we use a Schrödinger-picture formalism in which traveling-wave fields are discretized into infinitesimal time bins. We suggest that dynamically coupled cavities provide a very useful tool for improving the performance of quantum devices relying on cavity-enhanced light-matter interactions such as single-photon sources and atomlike quantum memories with photon interfaces. As an example, we present simulation results showing that high-fidelity two qubit entangling gates may be constructed using any of the considered nonlinear interactions.

Large-scale Integration of Artificial Atoms in Hybrid Photonic Circuits: A central challenge in developing quantum computers and long-range quantum networks is the distribution of entanglement across many individually controllable qubits. Colour centres in diamond have emerged as leading solid-state 'artificial atom' qubits because they enable on-demand remote entanglement, coherent control of over ten ancillae qubits with minute-long coherence times and memory-enhanced quantum communication. A critical next step is to integrate large numbers of artificial atoms with photonic architectures to enable large-scale quantum information processing systems. So far, these efforts have been stymied by qubit inhomogeneities, low device yield and complex device requirements. Here we introduce a process for the high-yield heterogeneous integration of 'quantum microchiplets'—diamond waveguide arrays containing highly coherent colour centres—on a photonic integrated circuit (PIC). We use this process to realize a 128-channel, defect-free array of germanium-vacancy and silicon-vacancy colour centres in an aluminium nitride PIC. Photoluminescence spectroscopy reveals long-term, stable and narrow average optical linewidths of 54 megahertz (146 megahertz) for germanium-vacancy (silicon-vacancy) emitters, close to the lifetime-limited linewidth of 32 megahertz (93 megahertz). We show that inhomogeneities of individual colour centre optical transitions can be compensated in situ by integrated tuning over 50 gigahertz without linewidth degradation. The ability to assemble large numbers of nearly indistinguishable and tunable artificial atoms into phase-stable PICs marks a key step towards multiplexed quantum repeaters and general-purpose quantum processors.

Bright High-Purity Quantum Emitters in Aluminium Nitride Integrated Photonics: Solid-state quantum emitters (QEs) are fundamental in photonic-based quantum information processing. There is strong interest to develop high-quality QEs in III-nitride semiconductors because of their sophisticated manufacturing driven by large and growing applications in optoelectronics, high voltage power transistors, and microwave amplifiers. Here, we report the generation and direct integration of QEs in an aluminium nitride-based photonic integrated circuit platform. For individual waveguide-integrated QEs, we measure an off-chip count rate exceeding 6×104 counts per second (cps) (saturation rate $> 8.6 \times 104$ cps). In an unpatterned thin-film sample, we measure antibunching with $g(2)(0) \sim 0.05$ and photon count rates exceeding 8×105 cps (saturation rate $> 1 \times 106$ cps). Although spin and detailed optical linewidth measurements are left for future work, these results already show the potential for high-quality QEs monolithically integrated in a wide

range of III-nitride device technologies that would enable new quantum device opportunities and industrial scalability.

LIST OF SYMBOLS, ABBREVIATIONS, AND ACRONYMS

AFM	atomic force microscope
AFRL	Air Force Research Laboratory
AlN	aluminum nitride
CMOS	complementary metal oxide semiconductor
CW	continuous-wave
cps	counts per second
DBR	Distributed Bragg reflectors
EBL	electron-beam lithography
FDTD	finite-difference time-domain
FIB	focused ion beam
FWHM	full-width at half-maximum
GeV	germanium-vacancy
InP	indium phosphide
MZI	Mach–Zehnder interferometers
NA	numerical aperture
NV	nitrogen vacancy
OSA	optical spectrum analyzer
PIC	photonic integrated circuit
PL	photoluminescence
PNP	programmable nanophotonic processors
Q	quality factor
QE	quantum emitter
QMC	quantum microchiplet

RIT	Rochester Institute of Technology
SEM	scanning electron microscope
Si APD	Silicon avalanche photodetector
SiV	silicon-vacancy
SOI	silicon on insulator
TE	transverse electric
UV	ultraviolet
UV-vis	ultraviolet to visible